International Journal of Mechanical Sciences 309 (2026) 111002

Contents lists available at ScienceDirect

International Journal of Mechanical Sciences

journal homepage: www.elsevier.com/locate/ijmecsci

Extracting residual stresses from experiments through inverse methods

José A. Sanz-Herrera [a,*], Alain Goriely [b]

[a] Escuela Técnica Superior de Ingeniería, Universidad de Sevilla, Spain
[b] Mathematical Institute, University of Oxford, United Kingdom

ARTICLE INFO

Keywords:
Nonlinear mechanics
Biomechanics
Finite element method
Residual stress
Inverse methods
Experimental stress analysis

ABSTRACT

Residual stresses are stresses present in a body in the absence of loads. They are found universally in biological systems and play a key role in many industrial applications as they alter a body's effective material properties. Typically, in biomechanics, they are the result of growth, remodeling, or other active processes. In industry, they are the consequence of manufacturing processes such as welding, cooling, or quenching. To study the response of materials with residual stresses, their initial values must be known, and neglecting their contribution may lead to wrong predictions, even at the qualitative level. It is therefore crucial to estimate them. Residual stresses can be obtained by simulating the underlying physics using numerical methods, or using experimental setups. The former approach is limited by the amount of constitutive models and associated phenomenological parameters needed in the simulation. In the latter approach, residual stress quantification is restricted to a certain region and its accuracy is affected by noisy measurements. In this paper we propose an inverse approach to reconstruct residual stress fields using domain displacements as an input. This displacement field is measured during the motion of the sample when it is sectioned (divided) into different regions through cutting experiments that partially relieve stresses. We demonstrate through various examples that residual stress recovery is possible both for linear and nonlinear solids while the formulation is independent of the physics of the residual stress source. Our findings show accurate reconstructions of residual stress when sufficiently many cuts have been performed, with errors below 10% and 20% for the linear and nonlinear examples, respectively, even for high input errors in the strain field ($\mathcal{O}(40\%)$). This unique mixed numerical-experimental approach is also valid to improve the quantification of residual stress fields in existing experimental methods.

1. Introduction

Residual stresses are defined as the stresses present in a material in the absence of external loads or body forces [1]. The most dramatic and earliest description of a material with residual stresses is likely to be found in the Prince Rupert's drops first mentioned in 1625 in Mecklenburg [2]. These are glass structures formed by rapidly cooling a molten drop of glass in cold water. This quenching process creates distinctive tadpole-shaped objects with a bulbous head and a long, thin tail, and it endows them with remarkable mechanical properties due to extreme residual stress distributions. The outer surface of the drop cools and solidifies quickly, forming a compressive shell. The interior cools more slowly and contracts, inducing high tensile stresses within the core and balanced compressive stresses on the exterior. This compressive shell gives the head of the drop an extraordinary resistance to impact; it can withstand hammer blows without breaking. However, the structure is highly sensitive. Any small damage or breakage at the tail releases the internal tensile stress, resulting in rapid disintegration of the entire drop into fine powder, due to the stored elastic energy causing crack propagation [3]. It is for this remarkable combination of extreme hardness and fragility that these glass drops attracted attention around 1660 when they were introduced by Prince Rupert of the Rhine (1619–1682), a nephew of King Charles I of England. Although he did not invent the drop, he introduced it to the English court around 1660, where it became an object of curiosity. Remarkably, the basic mechanism leading to their behavior was already understood by Robert Hooke who studied them and provided beautiful illustrations of them in *Micrographia* [4].

Simpler everyday objects also inherit their mechanical properties from residual stresses. For instance, the spoke of a bicycle wheel are in tension, hardening the entire structure, and so are the strings of a tennis racquet. These examples were already given by Frank Cilley in 1901 when he developed one of the first theory of linear elasticity with initial stresses [5]. At a much bigger scale, initial stresses are also key in understanding the stability of solid planets and it is only recently that such

* Correspondence to: Camino de los descubrimientos s/n, 41092 Seville, Spain.
E-mail address: jsanz@us.es (J.A. Sanz-Herrera).

https://doi.org/10.1016/j.ijmecsci.2025.111002
Received 16 July 2025; Received in revised form 9 October 2025; Accepted 8 November 2025
Available online 10 November 2025

stresses have been properly taken into account [6]. More generally, these initial stressed states can implicate instability or accelerate the failure in structures [7]. On the engineering side, residual stresses are typically found in solids in all industrial applications involving cooling or quenching; as well as manufacturing and fabrication processes, such as joining techniques, i.e. welding, and surface treatments [8–10].

In biology, plant physiologists already understood early the role in internal forces in stabilizing stems. For instance, Sachs in 1875 [11] already described the importance of growth-induced longitudinal tissue tension in a stalk of rhubarb to improve its rigidity [12,13]. Similarly, it was well appreciated that residual stresses are important in shaping tissues and organs during morphogenesis [14], but it is through the seminal contribution of Y.C. Fung that physiologists started to fully appreciate the importance of residual stresses [15] and realized that they are the hallmark of living systems.

Given the importance of residual stresses both in industry and biology, it is no surprise that they have been studied extensively both theoretically (numerically) and experimentally [16,17]. The most popular method to quantify experimentally residual stresses in industrial structures is the hole-drilling technique. This method was first introduced by Mathar in 1934 [18] and is based on the localized stress release after a portion of the material is removed (drilled). This relief produces a reconfiguration (deformation) around the drilled hole which is usually measured by strain gauge rosettes [19–21] or digital image correlation (DIC) techniques [22–27]. The experimentally measured strain field is used as the input of analytical (linear and infinitesimal elasticity) solutions available for thin specimens [28]. Semianalytical solutions, complemented by finite elements simulations, are used when the analytical solution is not possible (e.g. thick specimens) [20,29,30]. Since its introduction in 1934, many advances and developments of the drill-hole test have been proposed [31] and the literature is vast (see the excellent review [32] and references therein where additional techniques for residual stress quantification are exposed, including nondestructive methods such as diffraction methods, i.e. X-ray, neutron, synchrotron radiation, ultrasound, and magnetic methods). The American Society for Testing Materials (ASTM) established a standard (ASTM E837-1981) in 1981 which, after several revisions, was finally accepted as a standardized testing method (ASTM E837-08) for the drilling measurement of residual stress [33].

Residual stresses in metallic solids and structures are usually high, so plastic deformations caused by the stress concentration induced by the hole can occur. This could lead to stress calculation errors and this issue has been addressed in several papers [34,35]. Furthermore, the principles of the hole-drilling test have been used as a standard to measure the stress state in loaded structures, or to estimate unknown external loads in a number of applications, including ancient structures [36]. However, damage induced during drilling, i.e. deterioration of mechanical properties of the material around the hole, has not been taken into consideration in drilling-hole analysis.

Recently, residual stress quantification has attracted the attention of many researchers, as it is present in novel additive manufacturing techniques, 3D printing of structures, and high performance alloys [37,38]. In particular, titanium powder metallurgy and additive manufacturing have emerged as a cost-efficient solution to build lightweight aerospace structures [39]. In these applications, the drilling-hole method is also applied to estimate residual stresses [40–42]. An alternative approach is to use the finite element analysis to simulate the physics of heat transfer phenomena in a given manufacturing technique, and subsequent computation of residual stress. For instance, Yang et al. [43] modeled a moving Gaussian laser heat source to obtain temperature distributions of Ti6Al4V alloys by means of a transient thermal analysis. In the same context, residual stresses were numerically obtained in Ti6Al4V using coupled thermal-mechanical finite element simulations [44–46]. There is also a vast literature dedicated to the numerical analysis and simulation of temperature-induced residual stresses such as welding [47–51] or forming processes [52,53]. The numerical methodology to compute residual stresses by modeling the physics involved in the process is referred in this paper as the *direct* or *forward* approach.

In biomechanics, residual stresses are the consequence of growth and remodeling processes, and they are known to be crucial to the proper function of tissues and organs and are precisely tuned and maintained through life [1]. As in industrial applications, residual stresses in tissues have been quantified both experimentally and numerically. The most popular method to experimentally measure residual stresses is the opening angle test, and was introduced by Fung in arteries more than three decades ago [54,55]. Since then, this assay, and slight modifications of this test, have been used to estimate uniform prestresses which feed growth models. For instance, measured residual stresses were used as input to study the effect of viscoleastcity in aortic soft tissues [56]. Diaz et al. [57] introduced measured residual stresses in a computational model to capture the whole aorta response under uniaxial and biaxial stress states and to reproduce the response of the whole aorta to internal pressure. Similarly, residual stresses from ring opening tests were used to numerically investigate how stress patterns change when the artery is subjected to standard physiological pressures [58]. Moreover, *forward* computation of residual stress and strains by means of simulations is also routine in computational biomechanics. To cite a few, Mastrofni [59] computed residual strains to perform a stress analysis of patient-specific atherosclerotic carotid vessels. This line of research concluded that the incorporation of residual strains is fundamental to obtain proper distribution of stress across the atherosclerotic wall. Rausch and Kuhl [60] also highlighted the importance of considering prestrain and residual stress in the study of soft biological membranes. The impact of growth, remodeling and derived residual strains have been investigated in a number of tissues, namely, growing skin [61–64], tumors [65–67], tendons [68,69], brain tissue [70,71], and cardiovascular tissues [72–83], and plants [12,84,85].

Experimental and forward computation of residual stress have a number of limitations. First, both drilling-hole and opening angle methods assume residual stress as homogeneous and restrict its quantification to the region around the hole(s) or ring(s) of the setup. Therefore, acquiring distribution patterns of residual stress fields along the specimen/tissue is extremely difficult from an experimental perspective. Second, forward computation of residual stress needs a number of additional constitutive models and associated phenomenological parameters. For instance, temperature-induced residual stress in solids involves modeling the heat source and plasticity mechanisms. Most of the related phenomenological parameters are temperature-dependent, and they are usually poorly fitted or barely estimated from the literature. On the other hand, growth and remodeling models of tissues require kinematic and kinetic equations of growth [1], which also include phenomenological parameters. In this case, most of these parameters are unmeasurable and have to be fitted indirectly if experimental data are available. For this reason, the predictive capability of such growth models is quite limited, and they have been used instead to test theories and hypothesis to generate knowledge about the implications of mechanics in biophysical processes.

Experimental outcomes from drilling-hole tests have been combined with numerical algorithms to improve the quality of the data. For instance, Gore and Nobre [86] used an inverse formulation based on Tikhonov regularization to obtain more accurate residual stress fields. Barile et al. [87] implemented a Gaussian process regression to quantify uncertainty and to smoothen residual stress fields without the need for further regularization. Although these studies refer to inverse approaches fed by experimental hole-drilling outcomes, they are not suited to obtain spatial residual stress field distributions along the tested specimen. Similarly, in biomechanics, very few studies combine experimental results with numerical methods to estimate residual stress distributions. Among the few, Badel et al. [88] tracked the opening motion of an incised piece of arterial tissue by means of DIC, and used

this data as input in a mixed computational-experimental approach to estimate 3D residual stress fields.

Inspired by the inverse formalisms to compute traction forces by cells in artificial substrates [89–100], and elastography [101–103]; we previously proposed an inverse approach to compute residual stress fields [104]. In this work, data regarding to biaxial testing, i.e. domain displacement fields and biaxial loads, were synthetically generated and used as input in an inverse algorithm. Results showed accurate residual stress for noisy input displacements. However, this methodology is limited to solids that exhibit a nonlinear behavior.

Here, an alternative approach to [104] is presented in order to address this limitation. We propose sectioning residual stressed samples and tracking the displacements to the cut (relief) configuration using DIC, for example. Then, using this information as input of the developed inverse algorithm, we show that residual stresses can be recovered. The methodology is tested synthetically, i.e. no experimental data were used, although noisy displacement fields were considered; and it was implemented in a couple of examples of application: (i) growth in a nonlinear tissue and (ii) a surface heat treatment in a linear Ti6Al4V alloy specimen. Results show that the accuracy of recovered residual stress fields improves when the number of cut regions (sections) increases. However, precise residual stress profiles were already obtained along the line of the incision for a single cut. This approach demonstrates the possibility to recover complex residual stress fields independently of the source of residual stress in linear/nonlinear solids.

The paper is structured as follows: The rationales of the proposed inverse formulation, numerical elaboration and computer implementation, are detailed in Section 2. The different examples of application devised to demonstrate the capability of the methodology to recover residual stresses at different conditions, are introduced in Section 3. Details about the model, simulation and additional results regarding the second case of study are given in an Appendix. Results are then presented in Section 4 and discussed in Section 5. Finally, some conclusions are drawn at the end of the paper in Section 6.

2. Inverse approach

We start with a simply/multiply connected elastic body that enjoys a residual stress state $\boldsymbol{\sigma}^0$ in the reference configuration $\mathcal{B}_0$. This residual stress state is partially released by means of a cutting or opening operation in $\mathcal{B}_0$, which yields to the cut configuration $\mathcal{B}_C$. Configuration $\mathcal{B}_C$ can be multiply connected (e.g. drill hole test), simply connected (e.g. opening angle test) or non connected (e.g. fully cut, divided domains). Although the formulation is generic for any of these configurations, the numerical examples are restricted to the latter case (see Fig. 1).

To recover the residual stress field $\boldsymbol{\sigma}^0$, we propose the following constrained and regularized inverse formulation:

$$\underset{\boldsymbol{\sigma}^0,\boldsymbol{u}^C}{\operatorname{argmin}} \quad \frac{1}{2}\|\boldsymbol{u}^C-\boldsymbol{u}^{C\star}\|_2^2+\frac{\lambda}{2}\int_{\mathcal{B}_0}\|\nabla_0\boldsymbol{\sigma}^0\|_2^2\mathrm{d}v \tag{1}$$

$$s.t.$$

$$\mathcal{W}^0(\boldsymbol{\sigma}^0,\delta\boldsymbol{\varepsilon}^0)=\int_{\mathcal{B}_0}\boldsymbol{\sigma}^0\cdot\delta\boldsymbol{\varepsilon}^0\mathrm{d}v=0 \tag{2}$$

$$\mathcal{W}^C(\boldsymbol{u}^C,\boldsymbol{\sigma}^0,\delta\boldsymbol{\varepsilon}^C)=\int_{\mathcal{B}_C}\boldsymbol{\sigma}^C(\boldsymbol{u}^C,\boldsymbol{\sigma}^0)\cdot\delta\boldsymbol{\varepsilon}^C\mathrm{d}v=0, \tag{3}$$

where $\mathcal{W}^0$ represents the virtual work developed by the residual stress $\boldsymbol{\sigma}^0$ with virtual strain field $\delta\boldsymbol{\varepsilon}^0$ in the reference configuration $\mathcal{B}_0$. Similarly, $\mathcal{W}^C$ represents the virtual work developed by real internal (remaining) stress $\boldsymbol{\sigma}^C$ with virtual strain $\delta\boldsymbol{\varepsilon}^C$, in the cut configuration $\mathcal{B}_C$. Note that the absence of body and external forces in both (2) and (3), and hence the absence of external virtual work, ensure that the residual stress fields $\boldsymbol{\sigma}^0$, $\boldsymbol{\sigma}^C$ are self-balanced in their respective configurations. λ represents the regularization parameter which multiplies a first-order Tikhonov term in (1). As $\delta\boldsymbol{\varepsilon}^0$, $\delta\boldsymbol{\varepsilon}^C$ are identified as

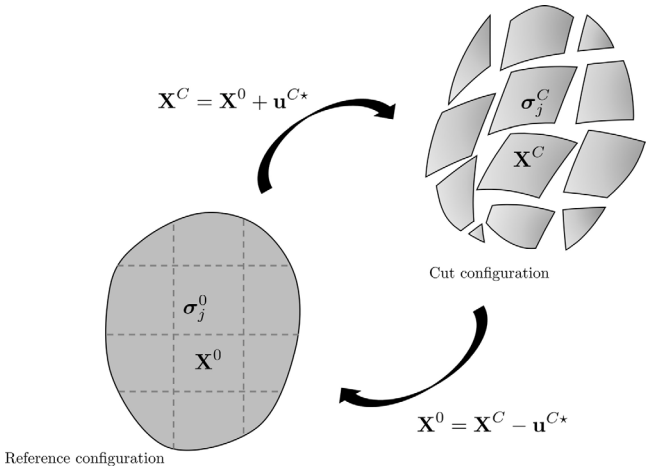

Fig. 1. Configurations used in the problem statement and numerical algorithm. The reference configuration $\mathcal{B}_0$ is incised/divided into a number of non connected domains (cuts in dashed lines) which yields the cut configuration $\mathcal{B}_C$, as the result of the (partial) release of residual stresses from $\boldsymbol{\sigma}_j^0$ to $\boldsymbol{\sigma}_j^C$. The motion of a material point $\mathbf{X}^0$ in the reference configuration to $\mathbf{X}^C$ in the cut configuration is characterized by the displacement field $\mathbf{u}^{C\star}$ (assumed as noisily measured). The illustration is represented for iteration j of the developed numerical scheme.

Lagrangian fields in Eqs. (2)–(3), $\mathcal{W}^0$ and $\mathcal{W}^C$ can be directly incorporated to the optimization Eq. (1) and then, its gradient obtained within the framework of a minimization searching algorithm (see additional details in [104]). However, this strategy yields complex and non-standard derivatives [104]. To circumvent this problem, we propose instead an iterative numerical algorithm divided into the following two subproblems: In the first subproblem, the input motion from the reference to the cut configurations is applied, while searching for a physically consistent stress field in this configuration. Conversely, in the second subproblem, the cut configuration is sent back to the reference configuration searching for a physically consistent stress field in the reference configuration. Both subproblems are solved recursively until convergence is achieved as follows.

Subproblem 1

First, we search for a physically consistent stress field $\boldsymbol{\sigma}^C$, while at the same time we minimize the distance between the computed and measured cut configurations, as follows:

$$\underset{\boldsymbol{\sigma}_{j+1}^C}{\operatorname{argmin}} \quad \frac{1}{2}\|\boldsymbol{\sigma}_{j+1}^C-\hat{\boldsymbol{\sigma}}_j^C(\boldsymbol{u}^{C\star},\boldsymbol{\sigma}_j^0)\|_2^2+\frac{\lambda}{2}\int_{\mathcal{B}_C}\|\nabla_C\boldsymbol{\sigma}_{j+1}^C\|_2^2\mathrm{d}v \tag{4}$$

$$s.t.$$

$$\mathcal{W}^C(\boldsymbol{\sigma}_{j+1}^C,\delta\boldsymbol{\varepsilon}_{j+1}^C)=\int_{\mathcal{B}_C}\boldsymbol{\sigma}_{j+1}^C\cdot\delta\boldsymbol{\varepsilon}_{j+1}^C\mathrm{d}v=0, \tag{5}$$

where $\hat{\boldsymbol{\sigma}}_j^C$ is a stress field that originates from the motion of the reference configuration (with residual stresses field $\boldsymbol{\sigma}_j^0$ from a previously converged iteration j, see overall algorithm in Box 1) to the cut configuration through measured displacement field $\boldsymbol{u}^{C\star}$ (see Fig. 1). Note that the stress field $\hat{\boldsymbol{\sigma}}_j^C$ is out of self-balance in the cut configuration, so the purpose of Eq. (4) is minimizing the distance from this field to a searched one $\boldsymbol{\sigma}_{j+1}^C$ which satisfies this condition through Eq. (5). Similarly to Eq. (1), λ represents a first order Tikhonov regularization parameter.

$\delta\boldsymbol{\varepsilon}_{j+1}^C$ in (5) can be interpreted as a Lagrangian field, so (5) can be included into Eq. (4) as follows:

$$\underset{\boldsymbol{\sigma}^C}{\operatorname{argmin}} \quad \pi=\frac{1}{2}\|\boldsymbol{\sigma}^C-\hat{\boldsymbol{\sigma}}^C\|_2^2+\frac{\lambda}{2}\int_{\mathcal{B}_C}\|\nabla_C\boldsymbol{\sigma}^C\|_2^2\mathrm{d}v+\int_{\mathcal{B}_C}\boldsymbol{\sigma}^C\cdot\delta\boldsymbol{\varepsilon}^C\mathrm{d}v. \tag{6}$$

Note that Eq. (6) is written for iteration j, and this index is omitted to simplify the notation.

The continuum fields $\boldsymbol{\sigma}^C$ and $\delta\boldsymbol{u}^C$, being this quantity the virtual displacement field derived from $\delta\boldsymbol{\varepsilon}^C$, are discretized and interpolated within each FE element as $\boldsymbol{\sigma}^C \approx \mathbf{N}_\sigma^C \cdot \boldsymbol{\sigma}_i^C$ and $\delta\boldsymbol{u}^C \approx \mathbf{N}_u^C \cdot \delta\mathbf{u}_i^C$. $\boldsymbol{\sigma}_i^C$ and $\delta\mathbf{u}_i^C$ are discrete node-valued vectors, which contains the components of each (discrete) variable at the nodes i of the element. $\mathbf{N}_\sigma^C$ and $\mathbf{N}_u^C$ are the corresponding shape (interpolating) functions within the element referred to the discretized cut configuration. Introducing this discretization into (6) yields,

$$\underset{\boldsymbol{\sigma}^C}{\text{argmin}} \quad \pi = \frac{1}{2}(\boldsymbol{\sigma}_i^C - \hat{\boldsymbol{\sigma}}_i^C)^\top \cdot (\boldsymbol{\sigma}_i^C - \hat{\boldsymbol{\sigma}}_i^C) + \\ + \frac{\lambda}{2}\sum_{k=1}^{NE}\left(\int_{\mathcal{B}_{C,k}} (\mathbf{B}_\sigma^C \cdot \boldsymbol{\sigma}_i^C)^\top \cdot (\mathbf{B}_\sigma^C \cdot \boldsymbol{\sigma}_i^C)\mathrm{d}v\right) + \mathcal{W}^C(\boldsymbol{\sigma}_i^C, \delta\mathbf{u}_i^C), \tag{7}$$

where $\mathbf{B}_\sigma^C$ is the gradient matrix of interpolating shape function matrix $\mathbf{N}_\sigma^C$ of the element k in the cut (discretized) configuration $\mathcal{B}_{C,k}$. NE is the number of elements of the FE mesh. In addition, we have

$$\mathcal{W}^C(\boldsymbol{\sigma}_i^C, \delta\boldsymbol{u}_i^C) = \sum_{k=1}^{NE}\left(\int_{\mathcal{B}_{C,k}} (\mathbf{N}_\sigma^C \cdot \boldsymbol{\sigma}_i^C \cdot \mathbf{B}_u^C \mathrm{d}v)^\top \cdot \delta\mathbf{u}_i^C\right) = (\mathbf{F}^{\text{int},C})^\top \cdot \delta\mathbf{u}^C, \tag{8}$$

where $\mathbf{F}^{\text{int},C}$ is the internal global vector of forces, after FE assembly operation. $\delta\mathbf{u}^C$ is a node-valued global vector which contains the components of the variables at each FE node of the mesh. Furthermore, assembly of (7) and introduction of (8) in (7) yields,

$$\underset{\boldsymbol{\sigma}^C}{\text{argmin}} \quad \pi = \frac{1}{2}(\boldsymbol{\sigma}^C - \hat{\boldsymbol{\sigma}}^C)^\top \cdot (\boldsymbol{\sigma}^C - \hat{\boldsymbol{\sigma}}^C) + \\ \frac{\lambda}{2}(\tilde{\mathbf{B}}_\sigma^C \cdot \boldsymbol{\sigma}^C)^\top \cdot \tilde{\mathbf{B}}_\sigma^C \cdot \boldsymbol{\sigma}^C + (\mathbf{F}^{\text{int},C})^\top \cdot \delta\mathbf{u}^C, \tag{9}$$

where $\tilde{\mathbf{B}}_\sigma^C$ is the global gradient matrix after assembly of element matrix $\mathbf{B}_\sigma^C$. $\boldsymbol{\sigma}^C$ and $\hat{\boldsymbol{\sigma}}^C$ are node-valued global vectors which contain the components of the variables at each FE node of the mesh. Eq. (9) has a minimum stationary solution at $\delta\pi(\boldsymbol{\sigma}^C, \delta\mathbf{u}^C) = \mathbf{0}$. Hence,

$$\boldsymbol{\sigma}^C - \hat{\boldsymbol{\sigma}}^C + \lambda\left(\tilde{\mathbf{B}}_\sigma^C\right)^\top \cdot \tilde{\mathbf{B}}_\sigma^C \cdot \boldsymbol{\sigma}^C + \left(\frac{\partial \mathbf{F}^{\text{int},C}}{\partial \boldsymbol{\sigma}^C}\right)^\top \cdot \delta\mathbf{u}^C, = \mathbf{0} \tag{10}$$

$$\mathbf{F}^{\text{int},C} = \mathbf{0}. \tag{11}$$

Eqs. (10)–(11) are written in matrix form as:

$$\begin{bmatrix} \mathbf{1} + \lambda\tilde{\mathbf{B}}_\sigma^{C\top} \cdot \tilde{\mathbf{B}}_\sigma^C & \tilde{\mathbf{B}}_u^{C\top} \\ \tilde{\mathbf{B}}_u^C & \mathbf{0} \end{bmatrix} \cdot \begin{Bmatrix} \boldsymbol{\sigma}_{j+1}^C \\ \delta\mathbf{u}_{j+1}^C \end{Bmatrix} = \begin{Bmatrix} \hat{\boldsymbol{\sigma}}_j^C \\ \mathbf{0} \end{Bmatrix}, \tag{12}$$

where $\tilde{\mathbf{B}}_u^C$ is the global gradient matrix after assembly of element matrices in (8). Note that Eq. (12) is linear with respect to $\boldsymbol{\sigma}^C$ and $\delta\mathbf{u}^C$ so it is solved in a single step.

Subproblem 2

Analogous to the first subproblem, we search here for a physically consistent stress field $\boldsymbol{\sigma}^0$, minimizing the distance between the computed and measured cut configurations:

$$\underset{\boldsymbol{\sigma}_{j+1}^0}{\text{argmin}} \quad \frac{1}{2}\|\boldsymbol{\sigma}_{j+1}^0 - \hat{\boldsymbol{\sigma}}_j^0(\boldsymbol{u}^{C\star}, \boldsymbol{\sigma}_j^C)\|_2^2 + \frac{\lambda}{2}\int_{\mathcal{B}_0} \|\nabla_C \boldsymbol{\sigma}_{j+1}^0\|_2^2 \mathrm{d}v \tag{13}$$

$$s.t.$$

$$\mathcal{W}^0(\boldsymbol{\sigma}_{j+1}^0, \delta\boldsymbol{\varepsilon}_{j+1}^0) = \int_{\mathcal{B}_0} \boldsymbol{\sigma}_{j+1}^0 \cdot \delta\boldsymbol{\varepsilon}_{j+1}^0 \mathrm{d}v = 0. \tag{14}$$

$\hat{\boldsymbol{\sigma}}_j^0$ is the stress field resulting from the motion of the cut configuration (with remaining stress field $\boldsymbol{\sigma}_j^C$ from a previously converged iteration j in subproblem 1, see additionally overall algorithm in Box 1) to the reference configuration through measured displacement field $-\boldsymbol{u}^{C\star}$ (see Fig. 1). Analogously to subproblem 1, the stress field $\hat{\boldsymbol{\sigma}}_j^0$ is not in self-balance in the reference configuration, so the purpose of Eq. (13) is to minimize the distance from this field to a searched one $\boldsymbol{\sigma}_{j+1}^0$ which satisfies this condition through Eq. (14). λ is the regularization parameter, assumed as the same than that of subproblem 1. This parameter will be calibrated in our study following the $L-$curve criterion [105].

Eq. (14) is introduced into Eq. (13) for a fixed iteration j as follows:

$$\underset{\boldsymbol{\sigma}^0}{\text{argmin}} \quad \pi = \frac{1}{2}\|\boldsymbol{\sigma}^0 - \hat{\boldsymbol{\sigma}}^0\|_2^2 + \frac{\lambda}{2}\int_{\mathcal{B}_0} \|\nabla_0 \boldsymbol{\sigma}^0\|_2^2 \mathrm{d}v + \int_{\mathcal{B}_0} \boldsymbol{\sigma}^0 \cdot \delta\boldsymbol{\varepsilon}^0 \mathrm{d}v. \tag{15}$$

Analogously to subproblem 1, the continuum fields in (15) are discretized and interpolated within each FE element as $\boldsymbol{\sigma}^0 \approx \mathbf{N}_\sigma^0 \cdot \boldsymbol{\sigma}_i^0$ and $\delta\boldsymbol{u}^0 \approx \mathbf{N}_u^0 \cdot \delta\mathbf{u}_i^0$. Then, the FE discretization and assembly procedures shown in subproblem 1 are performed here. So, the following system is obtained:

$$\begin{bmatrix} \mathbf{1} + \lambda\tilde{\mathbf{B}}_\sigma^{0\top} \cdot \tilde{\mathbf{B}}_\sigma^0 & \tilde{\mathbf{B}}_u^{0\top} \\ \tilde{\mathbf{B}}_u^0 & \mathbf{0} \end{bmatrix} \cdot \begin{Bmatrix} \boldsymbol{\sigma}_{j+1}^0 \\ \delta\mathbf{u}_{j+1}^0 \end{Bmatrix} = \begin{Bmatrix} \hat{\boldsymbol{\sigma}}_j^0 \\ \mathbf{0} \end{Bmatrix}, \tag{16}$$

where $\tilde{\mathbf{B}}_\sigma^0$ and $\tilde{\mathbf{B}}_u^0$ are global gradient matrices obtained after assembly of element matrices analogous to subproblem 1. Again, Eq. (16) is linear, so it is solved in a single step.

Subproblems 1 and 2 are iteratively solved as explained in Box 1.

Box 1: Two-step algorithm for residual stress recovery.

0. Initialize variables:

   $\boldsymbol{\sigma}_{j=0}^0 = \mathbf{0}$.

   WHILE $\|\boldsymbol{\sigma}_{j+1}^0 - \boldsymbol{\sigma}_j^0\|/\|\boldsymbol{\sigma}_j^0\| <$ TOL

   1. SUBPROBLEM 1
      - Compute $\hat{\boldsymbol{\sigma}}_j^C$ by applying the motion $\mathbf{u}^{C\star}$ to the reference configuration (incised) mesh. This mesh is obtained by duplicating nodes along the cut lines. This reference configuration is pre-stressed with residual stresses $\boldsymbol{\sigma}_j^0$ obtained from previous step of subproblem 2.
      - Assemble matrices $\tilde{\mathbf{B}}_\sigma^C$ and $\tilde{\mathbf{B}}_u^C$ in the cut configuration (Eq. (12)).
      - Build the system (12) and solve to obtain $\boldsymbol{\sigma}_{j+1}^C$.
   2. SUBPROBLEM 2
      - Compute $\hat{\boldsymbol{\sigma}}_j^0$ by applying the motion $-\mathbf{u}^{C\star}$ from the cut to the reference configuration meshes. This cut configuration is pre-stressed with residual stresses $\boldsymbol{\sigma}_j^C$ obtained from previous step of subproblem 1.
      - Assemble matrices $\tilde{\mathbf{B}}_\sigma^0$ and $\tilde{\mathbf{B}}_u^0$ in the reference configuration (non-incised mesh) (Eq. (16)).
      - Build the system (16) and solve to obtain $\boldsymbol{\sigma}_{j+1}^0$.

   END WHILE
3. Obtain the final configuration and displacement field $\mathbf{u}^C$ by applying a relaxation step in the reference configuration (incised mesh), with an initial (converged) pre-stress $\boldsymbol{\sigma}^0$.

Note that in the algorithm above the computation of stresses (first item of subproblems 1 and 2, as well as point 3) requires the use of the constitutive law considered for the solid. The algorithm shown in Box 1 was implemented in Matlab. Point 3 of Box 1 was carried out using Abaqus Simulia.

3. Applications

To highlight the versatility of the methodology, and also the fact that recovery does not depend on the source of residual stress, we

consider two different applications. The first one is related to residual stresses in a tissue appearing as a consequence of development/growth and remodeling. The second example arises in surface heat treatments carried out in alloys during manufacture. The simulations to obtain the ground truth solution were carried out using Abaqus Simulia.

3.1. Growth in nonlinear tissues

As previously noted residual stresses in biological tissues arise from growth and remodeling under physiological or pathological conditions. Although existing phenomenological models are available in the literature to simulate growth in tissues, and subsequent residual strains and stresses; here, we use the following naive approach to compute ground truth residual stress distributions in order to get the input data of our algorithm.

First, a random (smooth) growth region is defined (Fig. 2(a)). In this region, an inhomogeneous and isotropic nonlinear growth process, characterized by a deformation gradient tensor $\boldsymbol{F}^g$ in 2D Cartesian coordinates, is defined:

$$\boldsymbol{F}^g = \begin{bmatrix} 1+\gamma & 0 \\ 0 & 1+\gamma \end{bmatrix}, \tag{17}$$

where the function γ is inhomogeneous and decays exponentially from the center to the boundary of the growth region (see Fig. 2(b)). Then, the initial configuration (Fig. 2(a)) is subject to a deformation defined by the multiplicative decomposition of the deformation gradient $\boldsymbol{F}^a \cdot \boldsymbol{F}^g$, where $\boldsymbol{F}^a$ is the motion from an intermediate stress-free configuration to the final configuration. The new reference configuration (deformed after growth) is shown in (Fig. 2(c)). Likewise, residual (Cauchy) stresses in the reference configuration (see Fig. 1) are obtained as:

$$\boldsymbol{\sigma}^0 = \frac{2}{J^a} \cdot \boldsymbol{F}^a \left[\frac{\partial \Psi(\mathbf{C})}{\partial \mathbf{C}} \right]_{\mathbf{C}=\mathbf{C}^a} \cdot \boldsymbol{F}^{a\top}, \tag{18}$$

with the right Cauchy–Green strain tensor $\mathbf{C}^a = \boldsymbol{F}^{a\top} \cdot \boldsymbol{F}^a$, and $J^a = \det(\boldsymbol{F}^a)$. In our study, we restrict our attention to 2D deformations by enforcing a plane-stress condition leading to an incompressible plane-stress neo-Hookean 2D law.

After growth, the reference configuration is opened through cuts. It is assumed that no damage is induced during sectioning. Moreover, since the solid is assumed to be elastic, and hence free of inelastic deformations, the deformations and stresses are independent of the order the cuts are made. Different cases, i.e. number of cuts, are considered in our study to check the performance and ability of our methodology to recover residual stress based on this procedure. These different cases are shown in Figs. 2(d)–(g). Note that, to avoid dealing with different meshes at the initial and reference configurations after growth, straight cuts were defined in the undeformed (initial) configuration (Fig. 2(a)), resulting into non-straight cut lines after growth in the reference configuration (Figs. 2(d)–(g)).

After cutting, the reference domain is divided into different regions where the residual stresses have been partially released. The associated Von Mises stresses, for the different considered cases, are shown in Fig. 3 in the deformed cut configuration. An inhomogeneous remaining stress distribution is observed with high values along the cuts. As expected, the amount of released stress increases with the number of cuts. Finally, the motion associated with the deformation state from the opened reference configuration to the cut configuration is shown in Fig. 4. Note that this motion, i.e. displacement field, is the key input in our recovery algorithm and needs to be obtained from the experimental setup (for instance by means of DIC). Therefore, this displacement field is assumed to be noisy and is modified as follows:

$$\mathbf{u}^{C\star} = \mathbf{u}^{C,GT} + \boldsymbol{\xi} \cdot \left\| \mathbf{u}^{C,GT} \right\|, \tag{19}$$

where $\mathbf{u}^{C\star}$ and $\mathbf{u}^{C,GT}$ are the noisy and ground truth displacement vectors, respectively, that contain the different components of the displacement field at each node of the FE mesh, $\boldsymbol{\xi}$ is a randomly valued vector that follows a Gaussian distribution $\mathcal{N}(0, s)$, with standard deviation s. Two different levels of noise are considered, referred to as *high* and *low* noise levels in the study. The corresponding strain fields are shown in Figs. 5 and 6.

3.2. Surface treatments in alloys

As a second example, we consider the heat treatment of surface as the source of residual stresses. Such a residual stress state usually arises in alloys as a consequence of manufacturing processes. In particular, we consider a thin plate made of Ti6Al4V alloy subjected to a heat source for a given time interval, see Fig. 7(a). A coupled thermal-mechanical transient simulation is performed to obtain both temperature and strain/stress distributions in the plate. Moreover, plasticity is accounted for and mechanical properties of the alloy are assumed to be temperature-dependent. Details of the model, simulation and additional results are given in Appendix.

As a consequence of the nonlinear expansion due to heat, and the development of plastic strains, a residual stress state develops in the plate that is computed by means of the *forward* simulation from first principles as outlined above. Then, this new reference (residual stressed) configuration is cut repeatedly as in the previous example (again we assume that no damage is induced during sectioning). The different cases are shown in Figs. 7(b)–(e).

Equivalent Von Mises stresses, for the different considered cuts and cases, are shown in Fig. 8 in the divided regions of the reference domain. As in the previous example, an inhomogeneous remaining stress distribution is observed along the cut regions in this figure, and the amount of released stress increases with the number of cut (opened) sections. The deformation state originating from opening the reference configuration to the cut configuration is represented in Fig. 9. This displacement field, which is the input of the recovery algorithm, is assumed also to be noisy in this example, and is corrupted according to (19). Likewise, two different levels of noise are considered, referred to as high and low noise levels in the study. Corresponding noisy strain fields are plotted in Figs. 10 and 11.

4. Results

Residual stress reconstructions, following the algorithm detailed in Box 1, are shown in this section for the two examples of applications of the study (see Section 3). For each case, the input of the algorithm is the tracked displacement field $\mathbf{u}^{C\star}$ of the motion from the stressed reference configuration to the cut configuration. The error associated to these displacement fields, assumed to be noisy, are computed using the following formula:

$$\text{Err E } (\%) = 100 \cdot \sqrt{\sum_{i=1}^{NE} \frac{\left(\varepsilon_{xx,i}^{C,GT} - \varepsilon_{xx,i}^{C\star}\right)^2 + \left(\varepsilon_{yy,i}^{C,GT} - \varepsilon_{yy,i}^{C\star}\right)^2 + \left(\varepsilon_{xy,i}^{C,GT} - \varepsilon_{xy,i}^{C\star}\right)^2}{\left(\varepsilon_{xx,i}^{C,GT}\right)^2 + \left(\varepsilon_{yy,i}^{C,GT}\right)^2 + \left(\varepsilon_{xy,i}^{C,GT}\right)^2}}, \tag{20}$$

where $\varepsilon_{xx,i}^{C,GT}, \varepsilon_{yy,i}^{C,GT}, \varepsilon_{xy,i}^{C,GT}$ and $\varepsilon_{xx,i}^{C\star}, \varepsilon_{yy,i}^{C\star}, \varepsilon_{xy,i}^{C\star}$ are the components of the strain tensor at each element i, derived from the ground truth and noisy displacement fields, respectively. NE is the number of elements of the FE mesh. The logarithmic strain tensor is used in (20) for the first example of application (Section 3.1), and the infinitesimal strain tensor for the second example of application (Section 3.2). These errors are shown in Tables 1 and 3 for the first and second examples of application, respectively. As can be seen, the order of magnitude of the input error in strains for the low noise case is 20%, and 40% for the high noise level case in both examples. To test the convergence of recovered stresses to the ground truth solution an input noise free case is also considered.

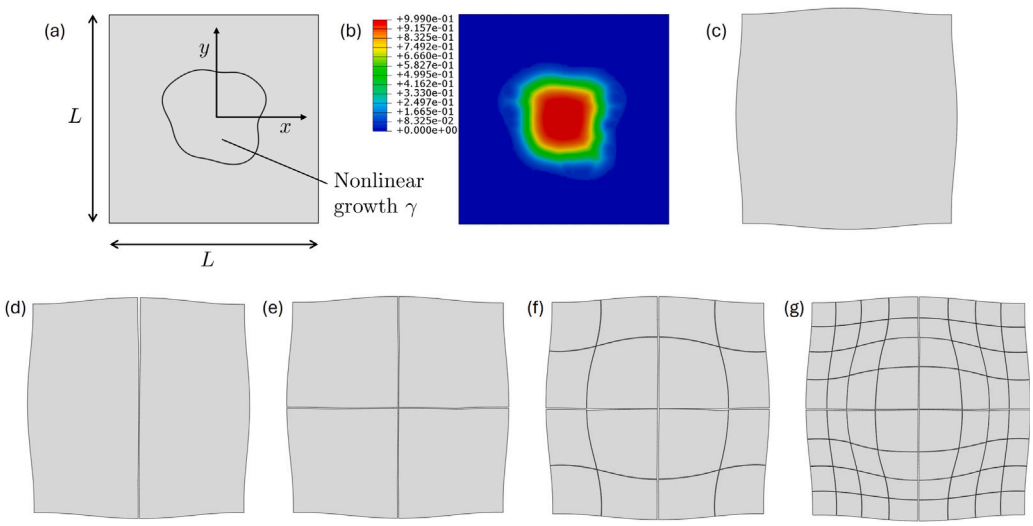

Fig. 2. First case: growth in nonlinear tissues. (a) Initial configuration and growth region. (b) Nonlinear growth function γ (see Eq. (17)). (c) Reference configuration obtained after growth. Then, this configuration is opened for study in a number of cases: (d) 2, (e) 4, (f) 16 and (g) 64 cut sections. Cuts are straight vertical and horizontal lines in the reference configuration leading to deformed pieces in the cut configuration.

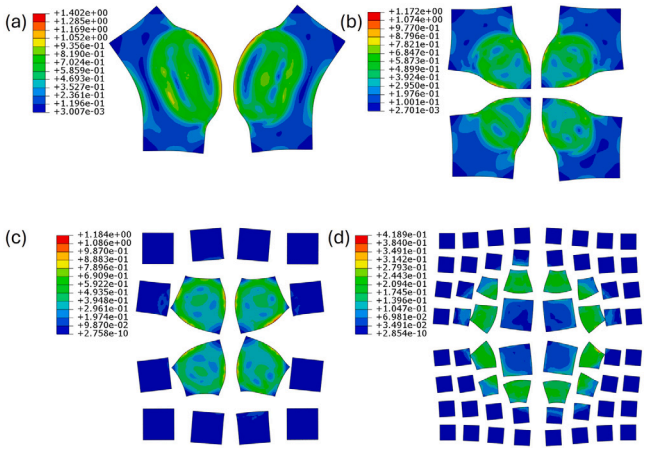

Fig. 3. Dimensionless equivalent Von Mises stresses (normalized by the Young's modulus) for the different considered cut cases in Figs. 2(d)–(g): (a) 2, (b) 4, (c) 16 and (d) 64 cut sections. Stresses are plot along the deformed cut regions and they represent partially released residual stress fields. Note the scale changes, showing a drastic reduction in stresses from a single cut to multiple cuts. Note that different color-scale limits are used in contour maps legends.

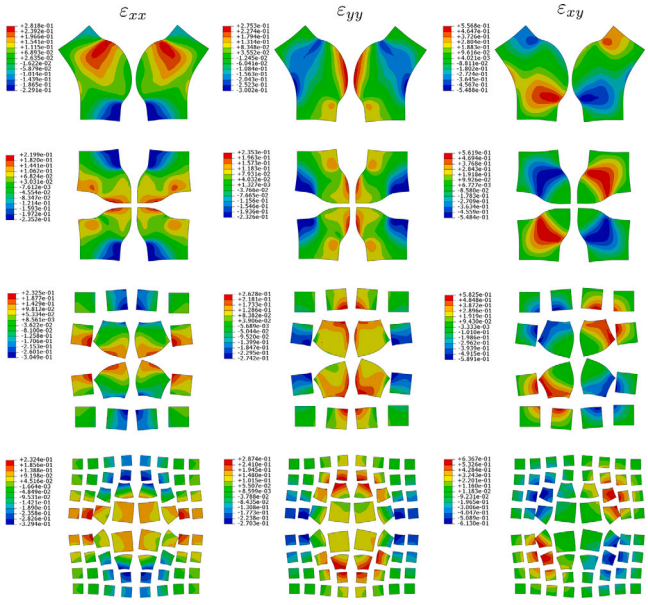

Fig. 4. Components of the logarithmic strain tensor for the different considered cut cases in Figs. 2(d)–(g): 2 (first row), 4 (second row), 16 (third row) and 64 (fourth row) cut sections. Strains are plot along the deformed cut sections. Note that different color-scale limits are used in contour maps legends.

Reconstructed residual stresses corresponding to the first example of application are shown in Fig. 12 using noise free displacement fields (associated strain fields plot in Fig. 4), in Fig. 13 using the low noise case displacement fields (associated strain fields plot in Fig. 5), and in Fig. 14 using the high noise case displacement fields (associated strain fields plot in Fig. 6). Quantitative residual stress recovery output errors are given in Table 1, based on the following formula:

$$\text{Err S}\ (\%) = 100 \cdot \sqrt{\sum_{i=1}^{NE} \frac{\left(\sigma_{xx,i}^{0,GT} - \sigma_{xx,i}^{0}\right)^2 + \left(\sigma_{yy,i}^{0,GT} - \sigma_{yy,i}^{0}\right)^2 + \left(\sigma_{xy,i}^{0,GT} - \sigma_{xy,i}^{0}\right)^2}{\left(\sigma_{xx,i}^{0,GT}\right)^2 + \left(\sigma_{yy,i}^{0,GT}\right)^2 + \left(\sigma_{xy,i}^{0,GT}\right)^2}}, \tag{21}$$

where $\sigma_{xx,i}^{0,GT}, \sigma_{yy,i}^{0,GT}, \sigma_{xy,i}^{0,GT}$ and $\sigma_{xx,i}^{0}, \sigma_{yy,i}^{0}, \sigma_{xy,i}^{0}$ are the components of the Cauchy's residual stress tensors at each element i, of the ground truth and recovered from input displacement fields, respectively. Note that the parameters regarding the iterative algorithm, such as number of iterations, CPU time, as well as the regularization parameter set in the simulations, are shown in Table 2.

Fig. 12 and Table 1 demonstrate that using noise free input displacements, the recovered stresses converge to the ground truth solution as the number of cuts increases. The same qualitative trend is observed in reconstructed stresses when the low noise level displacements (Fig. 13 and Table 1) and the high noise level displacements (Fig. 14 and Table 1) are used as inputs. It can be observed that outstanding/very good residual stress recovery are obtained using 64/16 cut regions (see Figs. 12–14), with reconstruction errors below 20% for the worst noise case. However, fair approximations are found for four cut regions case,

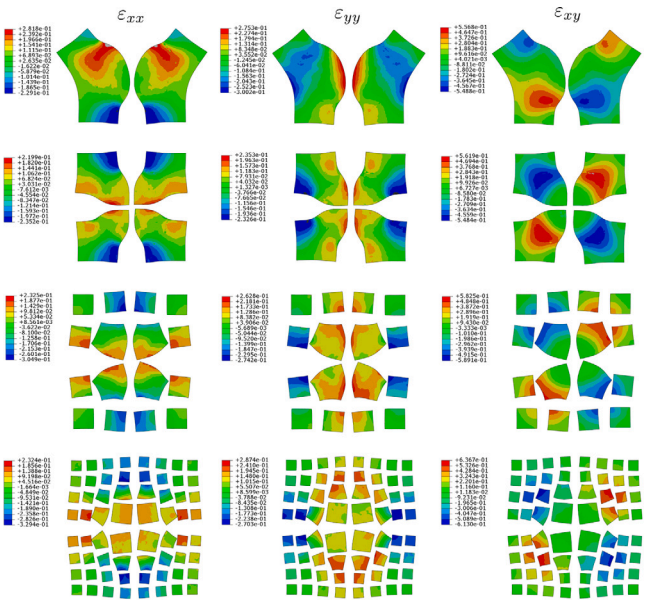

Fig. 5. Components of the logarithmic strain tensor, after adding noise to the ground truth displacement field (Eq. (19)), for the different considered cut cases in Figs. 2(d)–(g): 2 (first row), 4 (second row), 16 (third row) and 64 (fourth row) cut sections. Strains are plot along the deformed cut sections. Low noise level case. The overall error, versus the ground truth solution in Fig. 4, is shown for each case in Table 1. Note that different color-scale limits are used in contour maps legends.

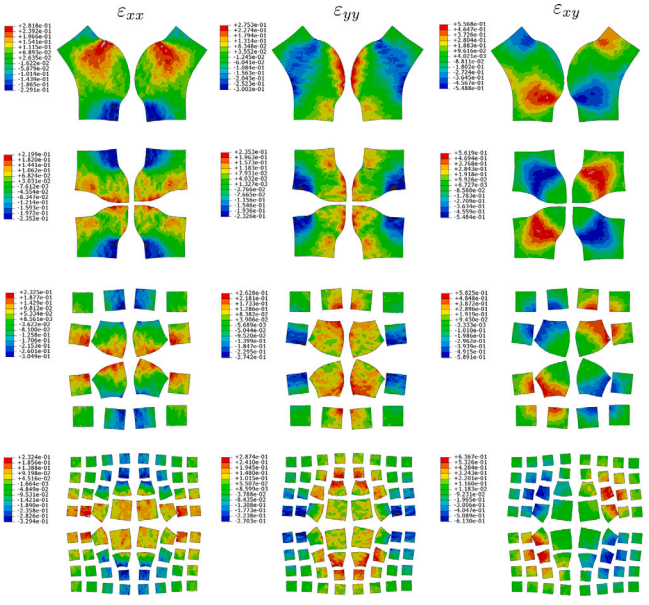

Fig. 6. Components of the logarithmic strain tensor, after adding noise to the ground truth displacement field (Eq. (19)), for the different considered cut cases in Figs. 2(d)–(g): 2 (first row), 4 (second row), 16 (third row) and 64 (fourth row) cut sections. Strains are plot along the deformed cut sections. High noise level case. The overall error, versus the ground truth solution in Fig. 4, is shown for each case in Table 1. Note that different color scale limits are used in contour maps legends.

whereas residual stress reconstructions provide high errors (> 30%) when the sample is cut in two sections under the presence of noise in the input displacements (see Table 1).

Reconstructed residual stresses corresponding to a surface heat treatment in a Ti6Al4V plate are shown in Fig. 15, using noise free

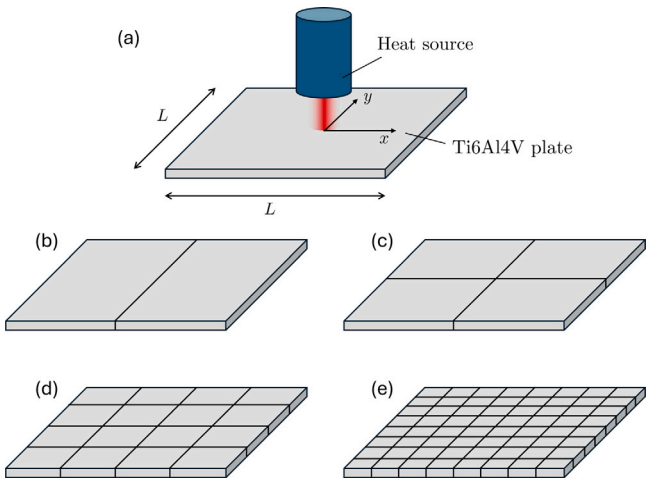

Fig. 7. Second example of application: surface heat treatment in alloys. (a) A heat source is applied on the surface of Ti6Al4V alloy plate. Subsequent residual stresses are computed by means of numerical simulation (details provided in Appendix). Then, this configuration is opened for study in a number of cases: (b) 2, (c) 4, (d) 16 and (e) 64 cut sections.

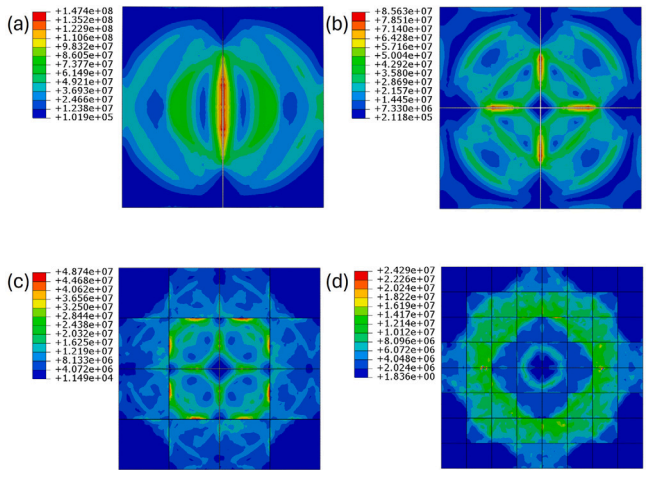

Fig. 8. Equivalent Von Mises stresses (Pa) for the different considered cut cases in Figs. 7(b)–(e): (a) 2, (b) 4, (c) 16 and (d) 64 cut regions. Stresses are plot along the cut sections and they represent partially released residual stress fields. Note that different color-scale limits are used in contour maps legends.

displacement fields (associated strain fields plot in Fig. 9), in Fig. 16 using the low noise case displacement fields (associated strain fields plot in Fig. 10), and in Fig. 17 using the high noise case displacement fields (associated strain fields plot in Fig. 11). Quantitative residual stress recovery output errors are given in Table 3, associated to the formula (21). Parameters regarding the iterative algorithm are shown in Table 4.

Similarly to stress reconstructions for the first example of application, the recovered stresses converge to the ground truth solution as the number of cuts increases (Fig. 15 and Table 3). Again, it can be observed that outstanding/very good residual stress recovery are obtained using 64/16 cut regions (see Figs. 15–17). However, in this example of application, very good results are obtained also for the four cut regions case with reconstruction errors below 20% for the worst noise case. (see Figs. 12–14 and Table 3). The recovered stress profile when the sample is cut in two regions deviates from the ground truth (see Figs. 15–17), with reconstruction errors of the order of 22%–25% versus the ground truth solution for different levels of noise (Table 3).

Table 1
Performance error metrics in the recovery of residual stress fields arising in growth in nonlinear tissues, for the different considered cut configurations. Err E represents the input error due to input noisy displacement fields, computed through Eq. (20). Err S represents the output error in residual stress reconstruction, computed through Eq. (21), using the proposed algorithm.

	Noise free		Low noise		High noise	
	Err E (%)	Err S (%)	Err E (%)	Err S (%)	Err E (%)	Err S (%)
64 sections	0	4.84	19.41	10.28	35.25	11.66
16 sections	0	8.02	16.07	16.27	34.01	18.40
4 sections	0	11.59	18.15	23.19	35.43	24.74
2 sections	0	15.22	18.44	33.30	38.68	36.05

Table 2
Parameters and numerical outputs in the simulations used for the recovery of residual stress fields arising in growth in nonlinear tissues, for the different considered cut configurations. λ is the regularization parameter used in the simulations. The second column refers to the number of passes (iterations) in the algorithm through subproblems 1 and 2 (Box 1). The third column shows the mean CPU time per iteration during the simulations. FE mesh contains 10012 triangular elements with linear interpolation and 5151 nodes (without counting duplicates nodes in cuts). Simulations were run in a laptop PC Intel i7 1.30 GHz, 16 GB RAM.

	Noise free			Low noise			High noise		
	λ	Iters	Time/iter (s)	λ	Iters	Time/iter (s)	λ	Iters	Time/iter (s)
64 sections	$2 \cdot 10^{-5}$	59	34.41	$2 \cdot 10^{-4}$	9	33.16	$3 \cdot 10^{-4}$	8	33.02
16 sections	$2 \cdot 10^{-5}$	61	33.08	$2 \cdot 10^{-4}$	11	33.04	$3 \cdot 10^{-4}$	7	34.50
4 sections	$2 \cdot 10^{-5}$	66	33.36	$2 \cdot 10^{-4}$	15	32.36	$7 \cdot 10^{-4}$	7	33.33
2 sections	$2 \cdot 10^{-5}$	109	35.81	$2 \cdot 10^{-4}$	19	35.80	$7 \cdot 10^{-4}$	7	34.53

Table 3
Performance error metrics in the recovery of residual stress fields arising in surface treatments in alloys, for the different considered cut configurations. Err E represents the input error due to input noisy displacement fields, computed through Eq. (20). Err S represents the output error in residual stress reconstruction, computed through Eq. (21), using the proposed algorithm.

	Noise free		Low noise		High noise	
	Err E (%)	Err S (%)	Err E (%)	Err S (%)	Err E (%)	Err S (%)
64 sections	0	3.54	19.03	5.97	37.23	7.61
16 sections	0	4.94	18.48	7.30	38.90	9.63
4 sections	0	10.27	18.69	11.10	38.50	15.55
2 sections	0	22.56	19.17	23.59	34.61	25.3

Table 4
Parameters and numerical outputs in the simulations regarding the recovery of residual stress fields arising in surface treatments in alloys, for the different considered cut configurations. λ is the regularization parameter used in the simulations. The second column refers to the number of passes (iterations) in the algorithm through subproblems 1 and 2 (Box 1). The third column shows the mean CPU time per iteration during the simulations. FE mesh contains 10012 triangular elements with linear interpolation and 5151 nodes (without counting duplicates nodes in cuts). Simulations were run in a laptop PC Intel i7 1.30 GHz, 16 GB RAM.

	Noise free			Low noise			High noise		
	λ	Iters	Time/iter (s)	λ	Iters	Time/iter (s)	λ	Iters	Time/iter (s)
64 sections	$5 \cdot 10^{-8}$	26	18.45	$3 \cdot 10^{-7}$	9	18.50	$5 \cdot 10^{-7}$	7	18.55
16 sections	$5 \cdot 10^{-8}$	78	18.53	$3 \cdot 10^{-7}$	23	18.54	$5 \cdot 10^{-7}$	17	18.64
4 sections	$5 \cdot 10^{-8}$	88	18.52	$5 \cdot 10^{-7}$	46	18.68	$1 \cdot 10^{-6}$	24	18.57
2 sections	$5 \cdot 10^{-8}$	148	18.47	$5 \cdot 10^{-7}$	60	18.53	$1 \cdot 10^{-6}$	36	18.44

The analysis of the results provided by residual stress reconstruction for the nonlinear case (growth in nonlinear tissues) and the linear case (heat treatment in linear Ti6Al4V plate) provide interesting observations and comparisons. First, the linear case provide overall better reconstructions that the nonlinear one, as can be seen in Tables 1 and 3. Also, the trends in the recovered residual stresses with level of noise and number of cut sections are qualitative similar in the linear and nonlinear cases. For both examples, the reconstruction errors remain stable with different levels of noise, as seen in Tables 1 and 3. Furthermore, when the sample is cut in just two sections, residual stress results should only be used qualitatively. However, even in the worst reconstructions cases (two and four cut regions), we obtain very good reconstructions along the cut line, as can be seen in Figs. 18 and 19. These plots show that we recovered for the normal residual stresses along the cut lines for two and four cut regions, respectively. Very good results are obtained for all the analyzed noise levels for the nonlinear example, providing even better reconstructions for the linear example.

5. Discussion

Significance of the proposed methodology

The proposed methodology showed the ability to recover complex residual stress fields using a combined numerical (inverse) and experimental approach, with application to linear and nonlinear solids. It also demonstrated, through the selected examples of application,

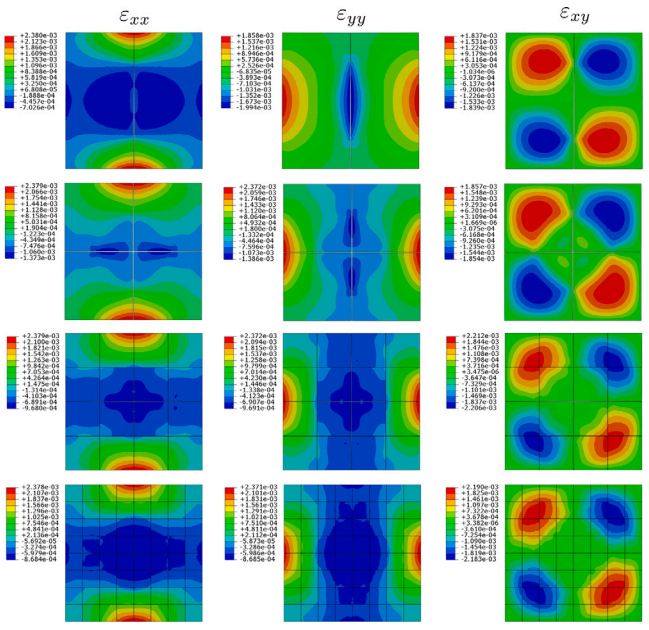

Fig. 9. Components of the logarithmic strain tensor for the different considered cut cases in Figs. 7(b)–(e): 2 (first row), 4 (second row), 16 (third row) and 64 (fourth row) cut sections. Strains are plot along the deformed cut sections. Note that different color-scale limits are used in contour maps legends.

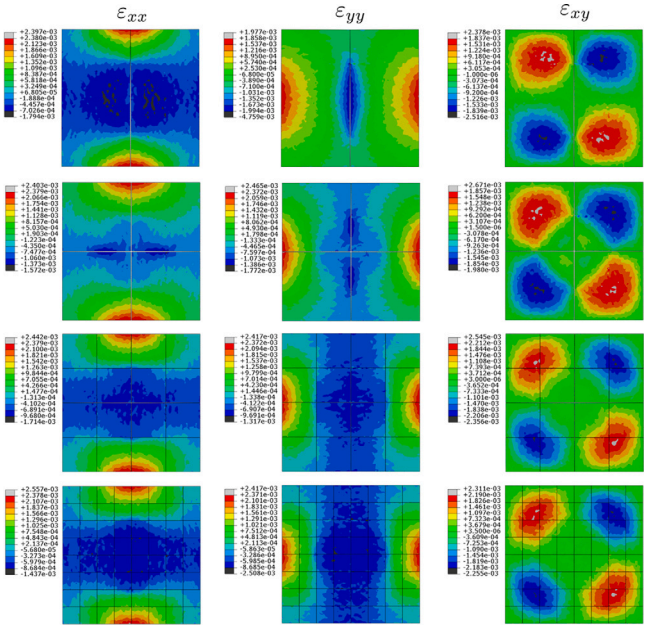

Fig. 10. Components of the strain tensor, after adding noise to the ground truth displacement field (Eq. (19)), for the different considered cut cases in Figs. 7(b)–(e): 2 (first row), 4 (second row), 16 (third row) and 64 (fourth row) cut sections. Strains are plot along the cut sections. Low noise level case. The overall error, versus the ground truth solution in Fig. 9, is shown for each case in Table 3. Note that different color-scale limits are used in contour maps legends.

the feasibility to reconstruct residual stress fields independently of the source of residual stress. This paper also improves the limitations of our previous work [104] in two ways: (i) it allows the recovery of residual stress in linear solids, and (ii) it introduces sectioning tests removing

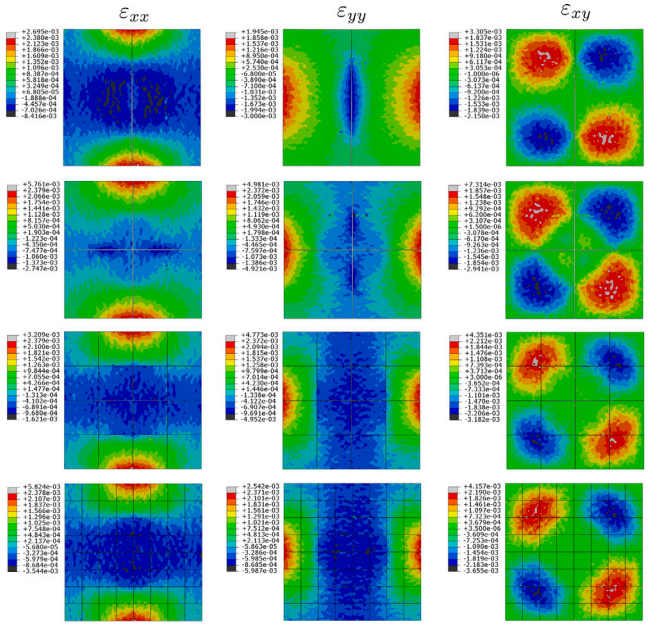

Fig. 11. Components of the strain tensor, after adding noise to the ground truth displacement field (Eq. (19)), for the different considered cut cases in Figs. 7(b)–(e): 2 (first row), 4 (second row), 16 (third row) and 64 (fourth row) cut sections. Strains are plot along the cut sections. High noise level case. The overall error, versus the ground truth solution in Fig. 9, is shown for each case in Table 3. Note that different color-scale limits are used in contour maps legends.

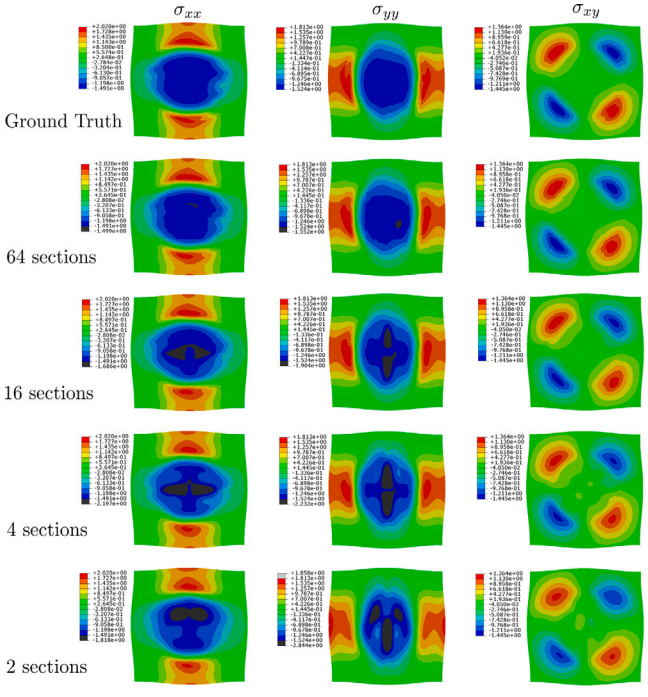

Fig. 12. Growth in nonlinear tissue (noise free input displacements): Dimensionless components (normalized by the Young's modulus) of the Cauchy's residual stress tensor in the reference configuration. The first row represents the ground truth solution for comparison purposes. Note that different color-scale limits are used in contour maps legends.

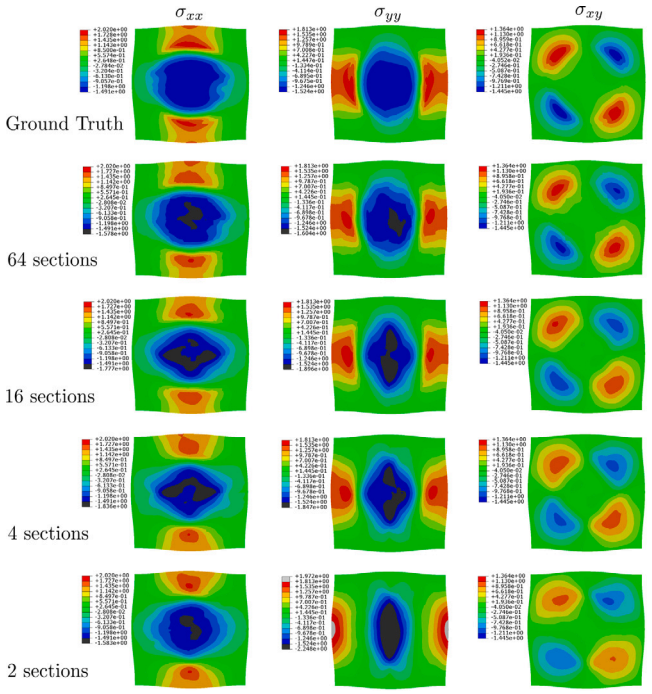

Fig. 13. Growth in nonlinear tissue (low noise level input displacements): Dimensionless components (normalized by the Young's modulus) of the Cauchy's residual stress tensor in the reference configuration. The first row represents the ground truth solution for comparison purposes. Note that different color-scale limits are used in contour maps legends.

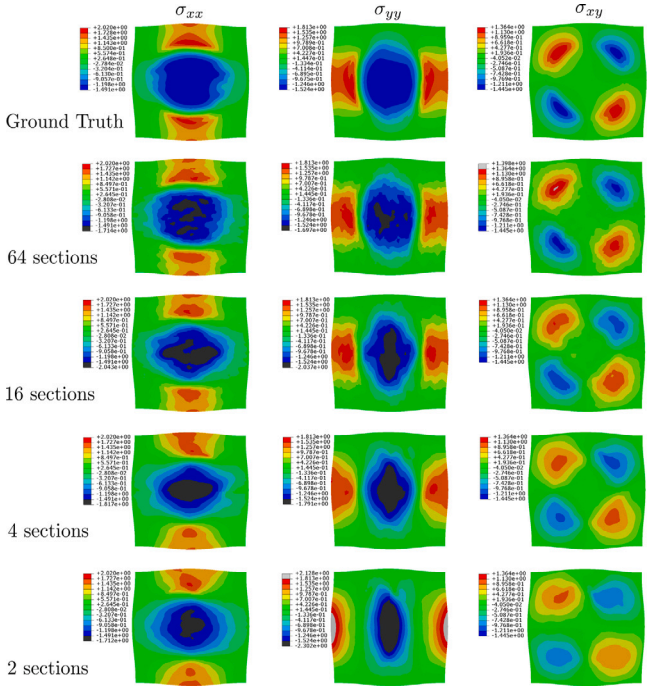

Fig. 14. Growth in nonlinear tissue (high noise level input displacements): Dimensionless components (normalized by the Young's modulus) of the Cauchy's residual stress tensor in the reference configuration. The first row represents the ground truth solution for comparison purposes. Note that different color-scale limits are used in contour maps legends.

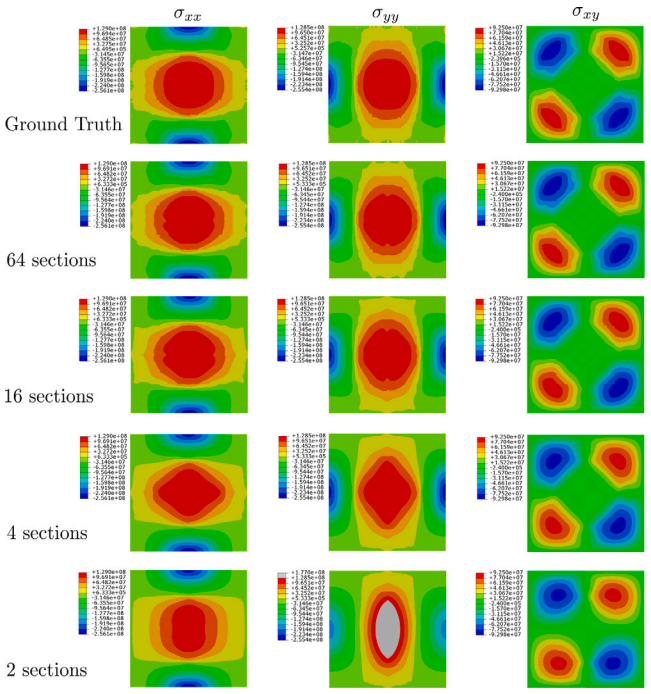

Fig. 15. Heat surface treatment in linear Ti6Al4V plate (noise free input displacements): Components of the Cauchy's residual stress tensor (Pa) in the reference configuration. The first row represents the ground truth solution for comparison purposes. Note that different color-scale limits are used in contour maps legends.

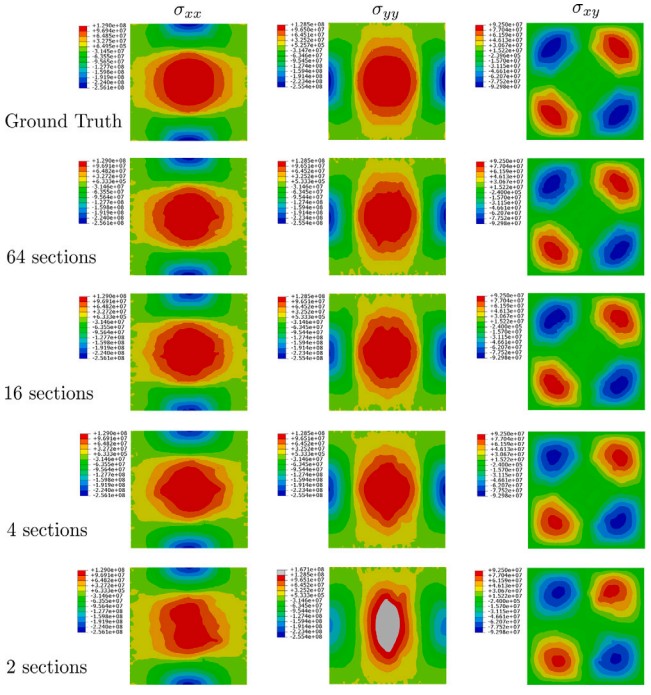

Fig. 16. Heat surface treatment in linear Ti6Al4V plate (low noise level input displacements): Components of the Cauchy's residual stress tensor (Pa) in the reference configuration. The first row represents the ground truth solution for comparison purposes. Note that different color-scale limits are used in contour maps legends.

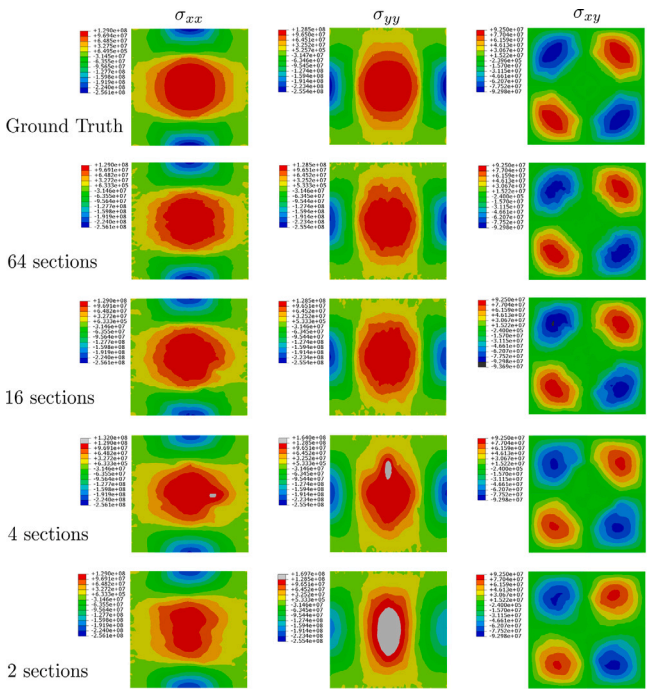

Fig. 17. Heat surface treatment in linear Ti6Al4V plate (high noise level input displacements): Components of the Cauchy's residual stress tensor (Pa) in the reference configuration. The first row represents the ground truth solution for comparison purposes. Note that different color-scale limits are used in contour maps legends.

biaxial assays, which is, a priori, a simplified experimental approach although partially destructive.

This unique mixed numerical-experimental approach complements existing methods to estimate residual stress in different applications. Notably, using minimal experimental feedback (i.e. displacement fields which can be routinely acquired by DIC), complex residual stress distributions can be obtained similar to outcomes provided by forward finite element simulations. However, as opposed to forward methods to compute residual stress, none phenomenological parameter is used in our formulation, which is particularly welcomed when complex physics are behind the computation of residual stress. For instance, computation of residual stress in the second example of application required 15 parameters after removing universal constants (see Appendix). 11 parameters are phenomenological, being 7 of them temperature-dependent (Appendix), which points out the difficulty to use forward simulations to get reliable residual stress fields. However, we believe that forward simulations are necessary in computation of residuals stress as far as the process of residual stress formation and related physics can be interpreted. In this context, our methodology can be used as a mean to further validate forward methods. It is important to remark at this point that even though our approach considers the physics of the source of residual stress as a blackbox, the obtained residual stress is physically consistent, as universal principles are imposed along the formulation.

The methodology proposed in this paper, established on a continuum framework, could be extended and/or adapted to incorporate machine learning and artificial intelligence elements, as recently proposed in different fields of the inverse problem [106,107].

Quality of recovered residual stress fields

As can be seen in Figs. 12–14 and Table 1 the quality of residual stress is very good, even for high levels of noise in the input displacement data, when 64/16 cut sections are used in the experiment for the nonlinear example. For the linear example, the quality of residual stress is also very good for four cut regions as can be seen in Figs. 15–17 and Table 3. It is therefore observed that residual stress recovery offers better results for the linear example, although the error in residual stress reconstructions remain stable for different levels of noise for all cases (see Tables 1 and 3). Reconstructions in which few cuts are used suffer the ill-posedness nature of inverse problems associated to noisy input quantities and non-uniqueness of the solution [105]. In the formulation shown in Section 3, the algorithm is guided by measured displacement field (equivalently strain field). It can be seen in Fig. 9, for example, that the input strain field is different depending on the number of sections, being more aligned with residual stress patterns as the number of cuts increases. Therefore, the accuracy of reconstructed residual fields is driven by input strain fields, which in turn, depends on the incisions and stress release in the cut configuration.

However, the worst case reconstructions, i.e. two and four cut regions, provided excellent residual stress profiles along the cuts, even for high levels of noise, as can be seen in Figs. 18 and 19. Since this is typically the region of highest stress, it suggests that our proposed methodology can be efficiently used to estimate residual stress profiles along selected/strategic incisions which, a priori, simplifies the experimental setup. Moreover, it paves the way to be explored in biomedical applications to analyze stress release in incised tissues, organs or in vitro setups.

In any case, we showed that the number of cuts influences stress-reconstruction accuracy suggesting that cut-layouts optimization might be a subject for future investigation.

Experimental setup

The developed numerical algorithm is driven by input displacement fields coming from the motion of sectioned samples as a consequence of the (partial) relief of residual stresses. It is assumed that no damage is induced in the cutting procedure, as is also assumed in drilling-hole and opening angle tests. As discussed, the quality of recovered residual stress fields improves with the number of cuts, something which might complicate the experimental protocol, requiring some kind of machine or tool in the setup. Specifically, rigid body motions when cut sections are put apart may be problematic during the DIC procedure. In this case, sections can be gripped, and a controlled displacement can be applied to circumvent this potential drawback. Sectioning experimental technique has also been implemented in metals as coupons tests (strips) in which released stress can be quantified [108].

Nonetheless, since our study is purely synthetic, it aims to stimulate experimentalists to devise methods and protocols in which this methodology could be applied. Our formulation could be easily adapted to single or multiply drilling-holes to improve existing numerical strategies in this test, as an alternative to the proposed experimental setup. In this case, the reference position is not lost during DIC as the resulting sample remains multiply connected.

This study was based on 2D samples and residual stress reconstructions were limited to 2D domains. In general, stresses can be relieved by 3D deformations after cuts, or can be applied to 3D specimens. In this context, experimental methods to obtain 3D input displacements fields are required. These methods rely on the measurement of displacements/deformations due to the release of residual stresses upon removal of material from the specimen, for example through recursive sectioning of the 3D specimen. This technique has been extensively used to study residual stresses in structural steel [109], aluminum [110] and stainless steel [111]; and it could be adapted here to our approach. For this purpose, the numerical algorithm shown in Box 1 would need to be adapted for 3D finite elements and meshes, resulting in an increase of the computational cost and potential mesh distortions during stress relief and related numerical instabilities. Future work includes exploration of these 3D environments using input surface displacements fields coming from the referred setups, and also drilling-holes and/or

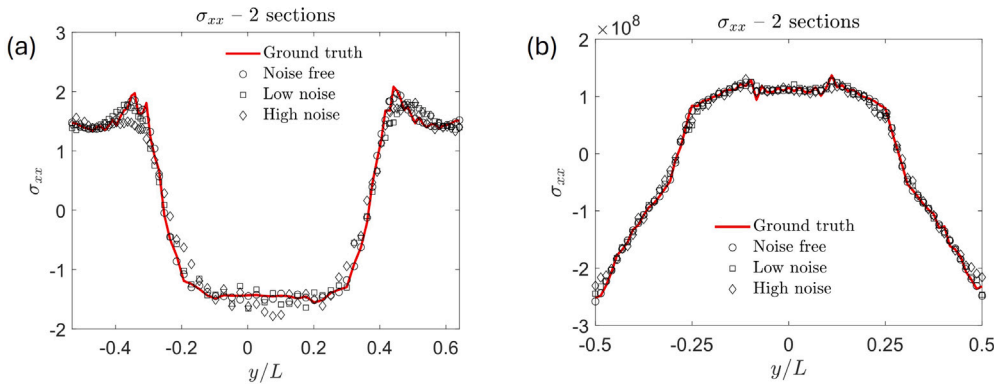

Fig. 18. Normal residual stresses along the cut line for two cut sections case (see Figs. 2 and 7) for all considered noise levels. (a) Normal residual stress (dimensionless value over the Young's modulus) for growth in nonlinear tissue example (see additionally reconstructed profiles in Figs. 12–14). (b) Normal residual stress (Pa) for heat treatment in linear Ti6Al4V plate example (see additionally reconstructed profiles in Figs. 15–17).

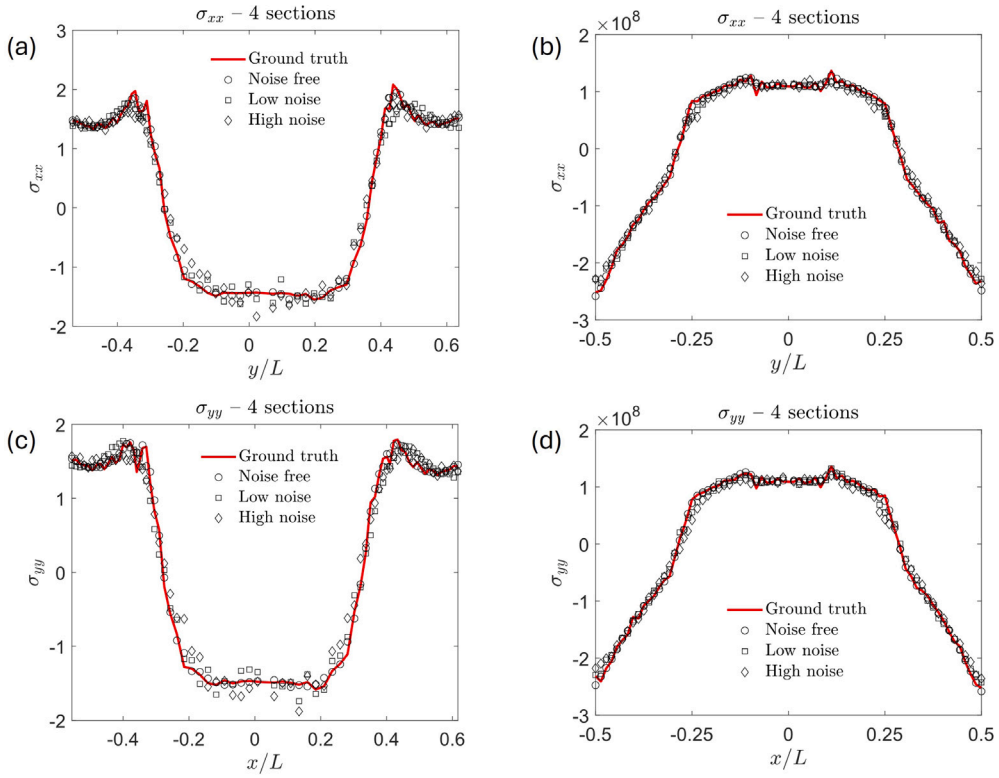

Fig. 19. Normal residual stresses along the cut lines for four cut sections cases for all considered noise levels. (a) Normal residual stress (dimensionless value normalized by the Young's modulus) along the vertical cut line (see Fig. 2) for growth in nonlinear tissue example (see additionally reconstructed profiles in Figs. 12–14). (b) Normal residual stress (Pa) along the vertical cut line (see Fig. 7) for heat treatment in linear Ti6Al4V plate example (see additionally reconstructed profiles in Figs. 15–17). (c) Normal residual stress (dimensionless value normalized by the Young's modulus) along the horizontal cut line (see Fig. 2) for growth in nonlinear tissue example (see additionally reconstructed profiles in Figs. 12–14). (d) Normal residual stress (Pa) along the horizontal cut line (see Fig. 7) for heat treatment in linear Ti6Al4V plate example (see additionally reconstructed profiles in Figs. 15–17).

partially incised specimens, both for industrial and biomechanical applications. Moreover, this inverse framework can be used to determine unknown distribution of stress states and loads to improve existing methods in this context.

6. Conclusion

We proposed a novel mixed numerical-experimental framework, combining inverse methods and continuum mechanics, for reconstructing residual stress fields. The approach is applicable to both linear and nonlinear solids with pre-existing stresses and is independent of the residual stress origin, as illustrated through diverse examples such as morphoelastic and thermoelastic stresses. Our algorithm uses domain displacement data arising from stress-relief processes, obtained by segmenting the specimen into separate, non-connected regions. This methodology builds upon established semi-destructive techniques, including sectioning, hole-drilling, and opening-angle methods; and it might be extended to incorporate machine learning elements. The robustness of our technique is demonstrated by examining displacement fields contaminated with varying noise levels, revealing stable reconstruction performance and enhanced accuracy as the number of subdivisions increases. Remarkably, precise residual stress profiles are consistently achieved along the cut interface, even when only a single incision is performed. Overall, our work opens the way for

the development of innovative experimental methodologies, thereby broadening the capabilities and precision of current residual stress analysis techniques.

CRediT authorship contribution statement

José A. Sanz-Herrera: Writing – review & editing, Writing – original draft, Software, Project administration, Methodology, Investigation, Funding acquisition, Formal analysis, Data curation, Conceptualization. **Alain Goriely:** Writing – review & editing, Writing – original draft, Resources, Methodology, Formal analysis, Conceptualization.

Declaration of competing interest

We the undersigned declare that this manuscript is original, has not been published before and is not currently being considered for publication elsewhere.

We confirm that the manuscript has been read and approved by all named authors and that there are no other persons who satisfied the criteria for authorship but are not listed. We further confirm that the order of authors listed in the manuscript has been approved by all of us.

We understand that the Corresponding Author is the sole contact for the Editorial process. He/she is responsible for communicating with the other authors about progress, submissions of revisions and final approval of proofs.

Acknowledgments

J.A.S.–H. was supported by the Salvador de Madariaga sabbatical fellowship of the Ministerio de Ciencia, Innovación y Universidades, Spain, grant number PRX22/00365, and MCIN/AEI/10.13039/501100011033 [PID2021-126051OB-C42].

Appendix. Simulation of surface heat treatment in Ti6Al4V plate

A surface heat treatment and subsequent residual stress in a square $L \times L$ plate ($L = 5$ cm) of Ti6Al4V alloy (Fig. 7(a)) are simulated as follows, assuming a 2D plane-stress analysis. A heat source (e.g. laser beam) is placed at the center of the plate, and the (transient) temperature distribution $T(\mathbf{x}, t)$ is obtained after solving the following equation:

$$\rho C_p \frac{\partial T(\mathbf{x},t)}{\partial t} + \nabla \cdot (\boldsymbol{\kappa} \cdot \nabla T(\mathbf{x},t)) = -q_r - q_v + q_{hs}(\mathbf{x},t) \qquad (A.1)$$
$$T(\mathbf{x},0) = T_0(\mathbf{x}) \ \in V,$$

where ρ and C_p are the alloy's density and specific heat, respectively. $\boldsymbol{\kappa}$ is the alloy's thermal conductivity tensor (assumed as isotropic, i.e. $\boldsymbol{\kappa} = \kappa \cdot \mathbf{I}$). The initial temperature distribution in the plate is assumed to be homogeneous $T(\mathbf{x}, 0) = T_0$. The right hand side of (A.1) represents surface fluxes including free (natural) air convection $q_v = h(T - T_0)$ (with h being the heat transfer or film coefficient), and radiation flux $q_r = \sigma\epsilon(T^4 - T_0^4)$ (with σ the Stefan–Boltzmann coefficient and ϵ the emissivity assuming grey body radiation). On the other hand, the surface heat source q_{hs} is modeled as follows [112]:

$$q_{hs}(\mathbf{x},t) = \begin{cases} \frac{4fAP}{\pi d_0^2} \exp\left[-4f\frac{\|\mathbf{x}\|_2^2}{d_0^2}\right] & t \le T_{hs} \\ 0 & t > T_{hs} \end{cases} \qquad (A.2)$$

where f is a (Gaussian) distribution factor, A the alloy's surface absorption (absorptivity), P the heat source power, and d_0 the heat source (laser beam) diameter. ρ, C_p κ are assumed to be temperature-dependent and they are taken from Ref. [113]. The rest of parameters (assumed as constant) are given in Table A.1. The temperature distribution coming from (A.1) was obtained in Abaqus Simulia, using the associated conditions and parameters exposed before. It is shown in Fig. A.1 for different time points from heating to cooling.

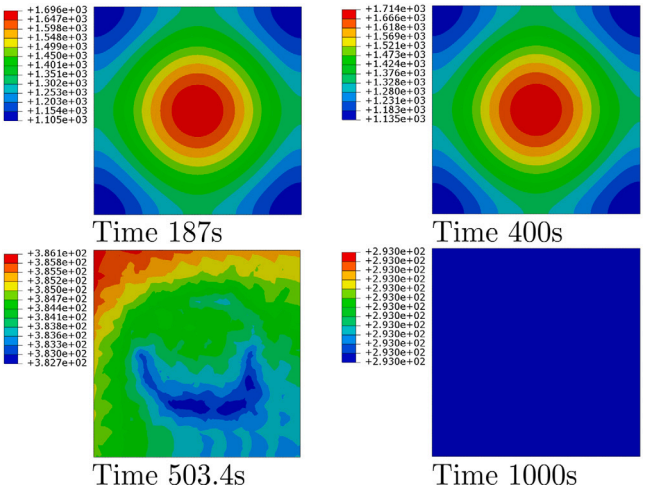

Fig. A.1. Temperature distribution (°K) in a square $L \times L$ plate ($L = 5$ cm) of Ti6Al4V alloy after solving Eq. (A.1) using Abaqus Simulia. The solution is shown for different time points from heating (time $\le$ 400 s) to cooling (time $>$ 400 s) after removing the heat source at time = 400 s. Note that different color scale limits are used in contour maps legends.

Table A.1
Parameters used in the heat transfer transient simulation according to Eqs. (A.1)–(A.2). The values and order of magnitude of the parameters were estimated from Refs. [43,112].

Parameter	Value
T_0 (°K)	293
h (W/m^2°K)	25
σ (W/m^2°K^4)	$5.67 \cdot 10^{-8}$
ϵ (–)	0.25
f (–)	2
A (–)	0.5
P (W)	150
d_0 (m)	$5 \cdot 10^{-2}$
T_{hs} (s)	400

The transient heat transfer analysis exposed above was then (weakly) coupled into a thermal-mechanical problem via strains due to material's expansion, according to inhomogeneous temperature distributions. A linear elastic model, followed by kinematic hardening plasticity, is assumed for the behavior of the Ti6Al4V alloy. The plastic regime is defined according to the Von Mises criterion. In this context, note that internal heat generation associated to plastic mechanisms were neglected in Eq. (A.1). Ti6Al4V Young's modulus, expansion coefficient, Yield stress and Poisson's ratio are considered to be temperature-dependent [113], as shown in Fig. A.2. The plate was free of body/surface forces and was not initially pre-stressed. The simulation was carried out using Abaqus Simulia. The different components of the plastic strains and stress tensors are shown in Figs. A.3–A.8 for different time points from heating to cooling. Note that residual stress distributions, used as the ground truth problem for this example of application, are shown at the last snapshot in Figs. A.6–A.8.

Data availability

Data will be made available on request.

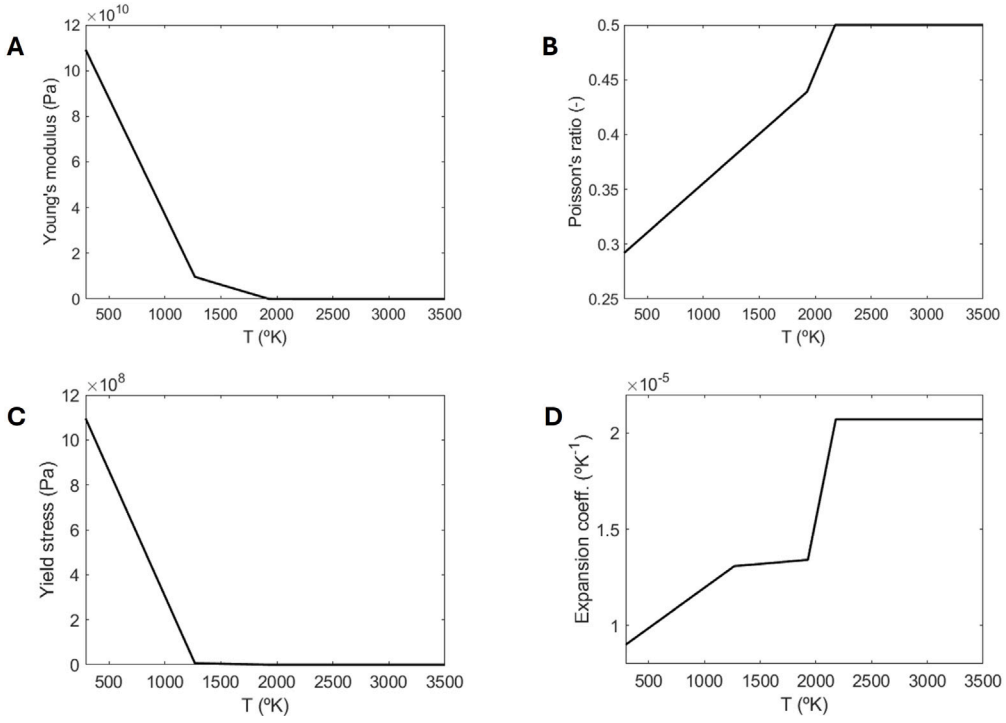

Fig. A.2. Temperature-dependent mechanical properties of Ti6Al4V alloy [113]. (A) Young's modulus, (B) Poisson's ratio, (C) yield stress and (D) expansion coefficient.

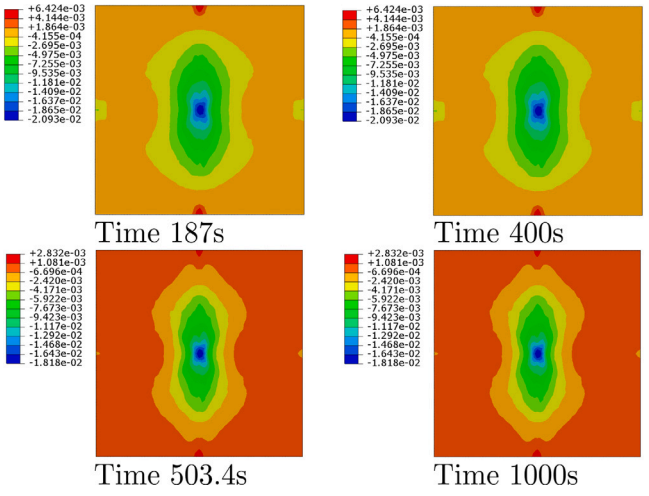

Fig. A.3. Plastic strain component ε_{xx}^{P} obtained from a coupled thermal-mechanical analysis (see temperature distributions shown in Fig. A.1). The solution is shown for different time points from heating (time ≤ 400 s) to cooling (time > 400 s) after removing the heat source at time = 400 s. Note that different color scale limits are used in contour maps legends.

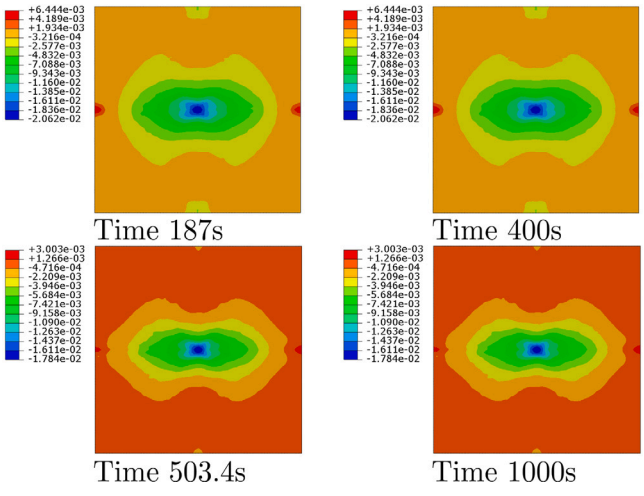

Fig. A.4. Plastic strain component ε_{yy}^{P} obtained from a coupled thermal-mechanical analysis (see temperature distributions shown in Fig. A.1). The solution is shown for different time points from heating (time ≤ 400 s) to cooling (time > 400 s) after removing the heat source at time = 400 s. Note that different color scale limits are used in contour maps legends.

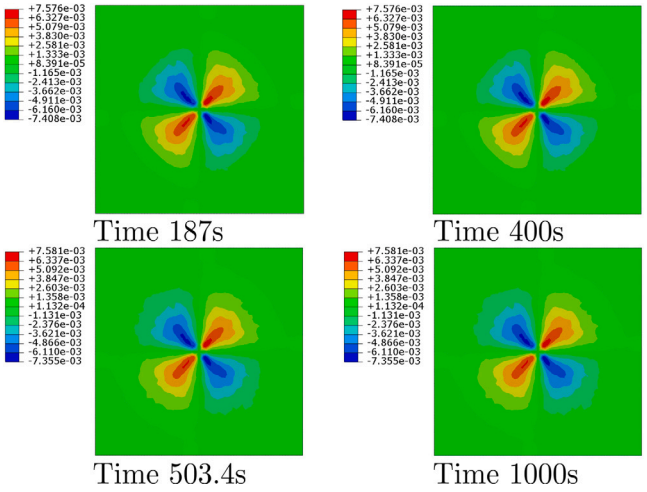

Fig. A.5. Plastic strain component ϵ_{xy}^{P} obtained from a coupled thermal-mechanical analysis (see temperature distributions shown in Fig. A.1). The solution is shown for different time points from heating (time ≤ 400 s) to cooling (time > 400 s) after removing the heat source at time = 400 s. Note that different color scale limits are used in contour maps legends.

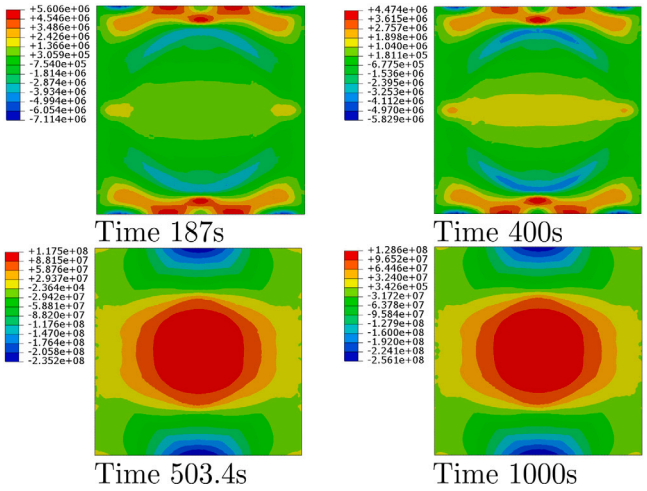

Fig. A.6. Stress component σ_{xx}^{P} (Pa) obtained from a coupled thermal-mechanical analysis (see temperature distributions shown in Fig. A.1). The solution is shown for different time points from heating (time ≤ 400 s) to cooling (time > 400 s) after removing the heat source at time = 400 s. Note that different color scale limits are used in contour maps legends.

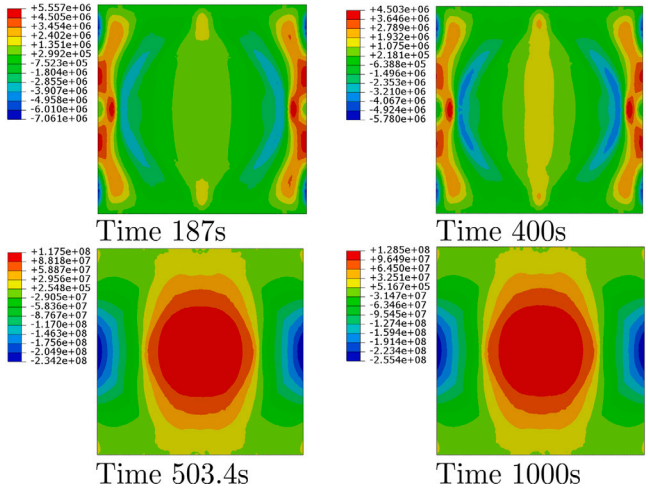

Fig. A.7. Stress component σ_{yy}^{P} (Pa) obtained from a coupled thermal-mechanical analysis (see temperature distributions shown in Fig. A.1). The solution is shown for different time points from heating (time ≤ 400 s) to cooling (time > 400 s) after removing the heat source at time = 400 s. Note that different color scale limits are used in contour maps legends.

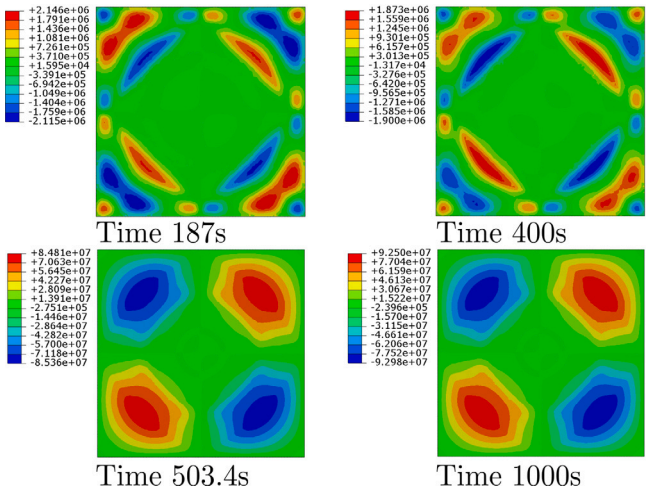

Fig. A.8. Stress component σ_{xy}^{P} (Pa) obtained from a coupled thermal-mechanical analysis (see temperature distributions shown in Fig. A.1). The solution is shown for different time points from heating (time ≤ 400 s) to cooling (time > 400 s) after removing the heat source at time = 400 s. Note that different color scale limits are used in contour maps legends.

References

[1] Goriely A. The mathematics and mechanics of biological growth. Springer; 2017.

[2] Brodsley L, Frank C, Steeds JW. Prince Rupert's drops. Notes and Records Roy Soc London 1986;41(1):1–26.

[3] Chaudhri MM. Explosive disintegration of thermally toughened soda–lime glass and prince rupert's drops. Phys Chem Glasses–Eur J Glas Sci Technol Part B 2006;47(2):136–41.

[4] Hooke R. Observation VII. of some phaenomena of glass drops. In: Micrographia or some physiological descriptions of minute bodies made by magnifying glasses with observation and inquiries thereupon. London; 1665, p. 33–44.

[5] Cilley FH. Fundamental propositions in the theory of elasticity; A study of primary or self-balancing stresses. Am J Sci 1901;4(64):269–90.

[6] Jia F, Kodio O, Chapman SJ, Goriely A. On the figure of elastic planets I: Gravitational collapse and infinitely many equilibria. Proc R Soc A 2019;475(2224):20180815.

[7] Mutafi A, Irwan JM, Yidris N, Alshalif AF, Saif Y, Abdulrahman H, et al. Residual stresses in cold-formed steel sections: An overview of influences and measurement techniques. Forces Mech 2025;18:100306.

[8] Leggatt RH. Residual stresses in welded structures. Int J Press Vessels Pip 2008;85:144–51.

[9] Chen C, Yin J, Zhu H, Xiao Z, Zhang L, Zeng X. Effect of overlap rate and pattern on residual stress in selective laser melting. Int J Mach Tools Manuf 2019;145:103433.

[10] Xiao Z, Chen C, Zhu H, Hua Z, Nagarajan B, Guo L, et al. Study of residual stress in selective laser melting of Ti6Al4V. Mater Des 2020;193:108846.

[11] Sachs J. Text-book of botany, morphological and physiological. Oxford: Clarendon; 1875.

[12] Vandiver R, Goriely A. Tissue tension and axial growth of cylindrical structures in plants and elastic tissues. Europhys Lett 2008;84(5):58004.

[13] Holland MA, Kosmata T, Goriely A, Kuhl E. On the mechanics of thin films and growing surfaces. Math Mech Solids 2013;18(6):561–75.

[14] Moore AR, Burt AS. On the locus and nature of the forces causing gastrulation in the embryos of *Dendraster excentricus*. J Exp Zool 1939;82(1):159–71.

[15] Chuong CJ, Fung YC. Residual stress in arteries. In: Frontiers in biomechanics. Springer; 1986, p. 117–29.

[16] Withers PJ, Bhadeshia HKDH. Residual stress. Part 1–measurement techniques. Mater Sci Technol 2001;17(4):355–65.

[17] Withers PJ, Bhadeshia HKDH. Residual stress. Part 2–nature and origins. Mater Sci Technol 2001;17(4):366–75.
[18] Mathar J. Determination of initial stresses by measuring the deformation around drilled holes. Trans ASME 1934;56:249–54.
[19] Rendler NJ, Vigness I. Hole-drilling strain-gauge method of measuring residual stresses. Exp Mech 1966;6:577–86.
[20] Schajer GS. Measurement of non-uniform residual stress using the hole-drilling method. J Eng Mater Technol 1988;110:338–49.
[21] Lakey MC, Hill MR. Validation of hole-drilling residual stress measurements in workpieces of various thickness. Exp Mech 2024;64:1529–44.
[22] McGinnis MJ, Pessiki S, Turker H. Application of three dimensional digital image correlation to the core-drilling method. Exp Mech 2005;45:359–67.
[23] Nelson DV, Makino A, Schmidt T. Residual stress determination using hole drilling and 3D image correlation. Exp Mech 2006;46:31–8.
[24] Lord JD, Penn D, Whitehead P. The application of digital image correlation for measuring residual stress by incremental hole drilling. Appl Mech 2008;1314:65–73.
[25] Gao J, Shang H. Deformation-pattern-based digital image correlation method and its application to residual stress measurement. Appl Opt 2009;48:1371–81.
[26] Winiarski B, Withers PJ. Micron-scale residual stress measurement by micro-hole drilling image correlation. Exp Mech 2012;52:417–28.
[27] Halabuk D, Vajdák M, Návrat T. Feasibility study of uniform residual stress measurement using the hole-drilling method and digital image correlation. Exp Mech 2025. http://dx.doi.org/10.1007/s11340-025-01226-6.
[28] Kirsch G. Theory of elasticity and application in strength of materials. Z Vevein Dtsch Ing 1898;42:797–807.
[29] Niku-Lari A, Lu J, Flavenot J. Measurement of residual-stress distribution by the incremental hole-drilling method. J Mech Work Technol 1985;11:167–88.
[30] Weinberg O, Vaclavik J, Jankovec J, Jaros P, Holy S. Experimental calibration of computational constants for hole drilling method. In: Gdoutos EE, editor. Experimental analysis of nano and engineering materials and structures. Dordrecht: Springer; 2007, p. 477–8.
[31] Kingston E, Stefanescu D, Mahmoudi A, Truman C, Smith D. Novel applications of the deep-hole drilling technique for measuring through-thickness residual stress distributions. J ASTM Int 2006;3:1–12.
[32] Guo J, Fu H, Pan B, Kang R. Recent progress of residual stress measurement methods: A review. Chin J Aeronaut 2021;34:54–78.
[33] ASTM E837-08. Standard test method for determining residual stresses by the hole-drilling strain-gage method. American Society for Testing and Materials; 2008.
[34] Lin YC, Chou CP. Error induced by local yielding around hole in hole drilling method for measuring residual stress of materials. J Mater Sci Technol 1995;11:600–4.
[35] Vangi D, Tellini S. Hole-drilling strain-gauge method: Residual stress measurement with plasticity effects. J Eng Mater Technol 2009;132:011003.
[36] Barrallo J, Zulueta A, Blanco L, Caro J, Sanchez-Beitia S. Stress measurements on ancient structures by the hole-drilling method. Exp Tech (SEM) 1994;19:9–13.
[37] Jia H, Sun H, Wang H, Wu Y, Wang H. Scanning strategy in selective laser melting (SLM): A review. Int J Adv Manuf Technol 2021;113:2413–35.
[38] Bera T, Mohanty S. A review on residual stress in metal additive manufacturing. 3D Print Addit Manuf 2024;11:1462–70.
[39] Dutta B, Froes FH. The additive manufacturing (AM) of titanium alloys. In: Qian M, Froes FH, editors. Titanium powder metallurgy. Butterworth-Heinemann; 2015, p. 447–68.
[40] Casavola C, Campanelli L, Pappalettere C. Experimental analysis of residual stresses in the selective laser melting process. In: Proceedings of the 11th international congress and exhibition on experimental and applied mechanics. Orlando, Fla, USA: Society for Experimental Mechanics; 2008, p. 1479–86.
[41] Salmi A, Atzeni E, Iuliano L, Manuela Galati M. Experimental analysis of residual stresses on AlSi10Mg parts produced by means of selective laser melting (SLM). Procedia CIRP 2017;62:458–63.
[42] Käß M, Weihe S, Werz M. Residual stress and distortion analysis of laser powder bed additive manufactured parts using the incremental hole drilling method and the cantilever method. J Adv Join Process 2025;12:100336.
[43] Yang J, Sun S, Brandt M, Yan W. Experimental investigation and 3D finite element prediction of the heat affected zone during laser assisted machining of Ti6Al4V. J Mater Process Technol 2010;210:2215–22.
[44] Gao S, Tan Z, Lan L, Lu G, He B. Experimental investigation and numerical simulation of residual stress and distortion of Ti6Al4V components manufactured using selective laser melting. J Mater Eng Perform 2022;31:8113–23.
[45] Ivanov S, Artinov A, Zemlyakov E, Karpov I, Rylov S, Em V. Spatiotemporal evolution of stress field during direct laser deposition of multilayer thin wall of Ti-6Al-4V. Materials 2022;15(263).
[46] Palmeri D, Pollara G, Licari R, Micari F. Finite element method in L-PBF of Ti-6Al-4V: Influence of laser power and scan speed on residual stress and part distortion. Metals 2023;13(1907).
[47] Goladk J, Chakravariti A, Bibby M. A new finite element model for welding heat sources. Metall Trans B 1984;15:299–305.
[48] Talijiat B, Radhakrishnan B, Zacharia T. Numerical analysis of GTA welding process with emphasis on post-solidification phase transformation effects on residual stress. Mater Sci Eng A 1998;246:45–54.
[49] Deng D. FEM prediction of welding residual stress and distortion in carbon steel considering phase transformation effects. Mater Des 2009;30:359–66.
[50] Liu C, Luo Z, He Y, Huang S, Tuo J, Ding H. Numerical simulation of welding residual stresses in 6082-T6 thin aluminum alloy. Measurement 2024;234:114800.
[51] Qin Y, Ma C, Mei L. Prediction of weld residual stresses based on numerical simulation and machine learning: A review. Int J Adv Manuf Technol 2025;138:2731–79.
[52] Waimeng Q, Jingguang T, Kwokfai C. Finite element predictions of residual stresses in cold-formed steel sections. Prog Steel Build Struct 2007;9:26–32.
[53] Guo H, Huang A, Xiong W, Xing S, Wang L, Zhang C, et al. Finite element simulation and residual stress analysis of the whole process of metal bellows forming. J Mater Eng Perform 2024;33:3758–69.
[54] Fung YC, Liu SQ. Change of residual strains in arteries due to hypertrophy caused by aortic constriction. Circ Res 1989;65:1340–9.
[55] Fung YC. What are the residual stresses doing in our blood vessels. Ann Biomed Eng 1991;19:237–49.
[56] Holzapfel GA, Sommer G, Auer M, Regitnig P, Ogden RW. Layer-specific 3D residual deformations of human aortas with non-atherosclerotic intimal thickening. Ann Biomed Eng 2007;35:530–45.
[57] Diaz C, Peña JA, Martinez MA, Peña E. Unraveling the multilayer mechanical response of aorta using layer-specific residual stresses and experimental properties. J Mech Behav Biomed Mater 2021;113:104070.
[58] Garcia-Herrera CM, Bustos CA, Celentano DJ, Ortega R. Mechanical analysis of the ring opening test applied to human ascending aortas. Comput Methods Biomech Biomed Engin 2016;19:1738–48.
[59] Mastrofni A, Marino M, Karlof E, Hedin U, Gasser TC. On the impact of residual strains in the stress analysis of patient-specific atherosclerotic carotid vessels: Predictions based on the homogenous stress hypothesis. Ann Biomed Eng 2024;52:1347–58.
[60] Rausch MK, Kuhl E. On the effect of prestrain and residual stress in thin biological membranes. J Mech Phys Solids 2013;61:1955–69.
[61] Socci L, Rennati G, Gervaso F, Vena P. An axisymmetric computational model of skin expansion and growth. Biomech Model Mechanobiol 2007;6:177–88.
[62] Tepole AB, Ploch CJ, Wong J, Gosain AK, Kuhl E. Growing skin: A computational model for skin expansion in reconstructive surgery. J Mech Phys Solids 2011;59:2177–90.
[63] Firouzi N, Garziera R, Holzapfel GA, Rabczuk T. Mechanics of finite nonlinear viscoelastic growth for soft biological tissues. Thin-Walled Struct 2025;210:112996.
[64] Laudo J, Han TH, Ledwon J, Figueroa AE, Gosain AK, Lee TK, et al. Predictive modeling of human skin deformation and growth during tissue expansion in postmastectomy breast reconstruction. J Bioemech Eng 2025;147:071002.
[65] Ambrosi D, Mollica F. On the mechanics of a growing tumor. Internat J Engrg Sci 2002;40:1297–316.
[66] Ballatore F, Lucci G, Giverso C. Modelling and simulation of anisotropic growth in brain tumours through poroelasticity: A study of ventricular compression and therapeutic protocols. Comput Mech 2024;74:1137–69.
[67] Chockalingam S, Cohen T. A large deformation theory for coupled swelling and growth with application to growing tumors and bacterial biofilms. J Mech Phys Solids 2024;187:105627.
[68] Garikipati K, Arruda EM, Grosh K, Narayanan H, Calve S. A continuum treatment of growth in biological tissue: The coupling of mass transport and mechanics. J Mech Phys Solids 2004;52:1595–625.
[69] Peña E, Calvo B, Martinez MA, Doblare M. A three-dimensional finite element analysis of the combined behavior of ligaments and menisci in the healthy human knee joint. J Biomech 2006;39:1686–701.
[70] Budday S, Steinmann P, Kuhl E. The role of mechanics during brain development. J Mech Phys Solids 2014;72:75–92.
[71] Budday S. Exploring human brain mechanics by combining experiments, modeling, and simulation. Brain Multiphysics 2023;5:100076.
[72] Taber LA, Humphrey JD. Stress-modulated growth, residual stress, and vascular heterogeneity. J Biomech Eng 2001;123:528–35.
[73] Goriely A, Vandiver R. On the mechanical stability of growing arteries. IMA J Appl Math 2010;75(4):549–70.
[74] Holzapfel GA, Ogden RW. Modelling the layer-specific three-dimensional residual stresses in arteries, with an application to the human aorta. J R Soc Int 2009;7:787–99.
[75] Humphrey J. Cardiovascular tissue mechanics: Cells, tissues, and organs. Springer; 2002.
[76] Kuhl E, Maas R, Himpel G, Menzel A. Computational modeling of arterial wall growth: Attempts towards patient-specific simulations based on computer tomography. Biomech Mod Mechanobiol 2007;6:321–31.
[77] Göktepe S, Abilez OJ, Parker KK, Kuhl E. A multiscale model for eccentric and concentric cardiac growth through sarcomerogenesis. J Theoret Biol 2010;265:433–42.

[78] Kroon W, Delhaas T, Arts T, Bovendeerd P. Computational modeling of volumetric soft tissue growth: Application to the cardiac left ventricle. Biomech Model Mechanobiol 2009;8. 301–309.
[79] Rausch MK, Dam A, Göktepe S, Abilez OJ, Kuhl E. Computational modeling of growth: Systemic and pulmonary hypertension in the heart. Biomech Model Mechanobiol 2011;10:799–811.
[80] Humphrey JD, Schwartz MA. Vascular mechanobiology: homeostasis, adaptation, and disease. Review of Biomedical Engineering 2021;23:1–27.
[81] Zhang W, Sommer G, Niestrawska JA, Holzapfel GA, Nordsletten D. The effects of viscoelasticity on residual strain in aortic soft tissues. Acta Biomater 2022;140:398–411.
[82] Breslavsky ID, Amabili M. Fitting mechanical properties of the aortic wall and individual layers to experimental tensile tests including residual stresses. J Mech Behav Biomed Maters 2023;138:105647.
[83] Tamura A, Matsumoto K. Effects of implemented residual stresses on mechanical responses and behavior of the full-layered murine aortic medial ring: A parametric finite element study. Cardiovasc Eng Technol 2025;16:91–107.
[84] Goriely A, Moulton DE, Vandiver R. Elastic cavitation, tube hollowing, and differential growth in plants and biological tissues. Europhys Lett 2010;91(1):18001.
[85] Oliveri H, Cheddadi I. Hydromechanical field theory of plant morphogenesis. J Mech Phys Solids 2025;196:106035.
[86] Gore B, Nobre J. Effects of numerical methods on residual stress evaluation by the incremental hole-drilling technique using the integral method. Mater Res Proc 2016;2:587–92.
[87] Barile C, Carone S, Casavola C, Pappalettera G. Implementation of Gaussian process regression to strain data in residual stress measurements by hole drilling. Measurement 2023;211:112590.
[88] Badel P, Genovese K, Avril S. 3D residual stress field in arteries: Novel inverse method based on optical full-field measurements. Strain 2012;48:528–38.
[89] Legant WR, Miller JS, Blakely BL, Cohen DM, Genin GM, Chen CS. Measurement of mechanical tractions exerted by cells in three dimensional matrices. Nature Methods 2010;7:969–71.
[90] Michel R, Peschetola V, Vitale G, Etienne J, Duperray A, Ambrosi D, et al. Mathematical framework for traction force microscopy. ESAIM: Proc 2013;42:61–83.
[91] Song D, Dong L, Gupta M, Li L, Klaas O, Loghin A, et al. Recovery of tractions exerted by single cells in three dimensional nonlinear matrices. J Biomech Eng 2020;(142).
[92] Sanz-Herrera JA, Barrasa-Fano J, Condor M, Van Oosterwyck H. Inverse method based on 3D nonlinear physically constrained minimisation in the framework of traction force microscopy. Soft Matter 2021;17:10210–22.
[93] Barrasa-Fano J, Shapeti A, de Jong J, Ranga A, Sanz-Herrera JA, Van Oosterwyck H. Advanced in silico validation framework for three dimensional traction force microscopy and application to an in vitro model of sprouting angiogenesis. Acta Biomater 2021;126:326–38.
[94] Apolinar-Fernandez A, Barrasa-Fano J, Condor M, Van Oosterwyck H, Sanz-Herrera JA. Traction force reconstruction assessment on real three dimensional matrices and cellular morphologies. Internat J Engrg Sci 2023;186:103828.
[95] Apolinar-Fernandez A, Barrasa-Fano J, Van Oosterwyck H, Sanz-Herrera JA. Multiphysics modeling of 3D traction force microscopy with application to cancer cell-induced degradation of the extracellular matrix. Eng Comput 2024.
[96] Song D, Seidl DT, Oberai AA. Three-dimensional traction microscopy accounting for cell-induced matrix degradation. Comput Methods Appl Mech Engrg 2020;364:112935.
[97] Schwarz US, Soine JRD. Traction force microscopy on soft elastic substrates: A guide to recent computational advances. Biochim Biophys Acta - Mol Cell Res 2015;1853:3095–104.
[98] Apolinar-Fernandez A, Blazquez-Carmona P, Ruiz-Mateos R, Barrasa-Fano J, Van Oosterwyck H, Reina-Romo E, et al. Regularization techniques and inverse approaches in 3D traction force microscopy. Int J Mech Sci 2024;283:109592.
[99] Apolinar-Fernández A, Barrasa-Fano J, Van Oosterwyck H, Sanz-Herrera JA. Inverse modeling of heterogeneous ECM mechanical properties in nonlinear 3DTFM. Eur J Mech A-Solids 2025;114:105722.
[100] Kandasamy A, Yeh YT, Serrano R, Mercola M, del Alamo JC. Uncertainty-aware traction force microscopy. PLoS Comp Biol 2025;21:e1013079.
[101] Goenezen A, Barbone P, Oberai AA. Solution of the nonlinear elasticity imaging inverse problem: The incompressible case. Comput Methods Appl Mech Engrg 2011;200:1406–20.
[102] Liu T, Babaniyi OA, Hall TJ, Barbone PE, Oberai AA. Noninvasive in-vivo quantification of mechanical heterogeneity of invasive breast carcinomas. PLoS One 2015;10(7):e0130258.
[103] Mei Y, Zhao DM, Xiao CJ, Sun Z, Zhang WS, Guo X. Nondestructively identifying the mechanical behavior of soft tissues using surface deformation with an explicit inverse approach. Appl Math Model 2024;134:126–47.
[104] Sanz-Herrera JA, Goriely A. Physics-informed recovery of nonlinear residual stress fields in an inverse continuum framework. J Mech Phys Solids 2025;200:106079.
[105] Vogel CR. Computational methods for inverse problems. Philadelphia, PA, USA: Society for Industrial and Applied Mathematics; 2002.
[106] Chen W, Chen J, Guo W. Deep learning methods for solving linear inverse problems: Research directions and paradigms. Signal Process 2020;177:107729.
[107] Ying L. Solving inverse problems with deep learning. International Mathematical Union, EMS Press; 2021, p. 5154–75.
[108] Cruise RB, Gardner L. Residual stress analysis of structural stainless steel sections. J Constr Steel Res 2008;64:352–66.
[109] Estuar FR, Tall L. Experimental investigation of welded built-up columns. Weld Res Suppl 1963;42:164–75.
[110] Mazzolani FM. Aluminium alloy structures. 2nd ed.. An imprint of Chapman and Hall; 1995.
[111] Young B, Lui WM. Behavior of cold-formed high strength stainless steel sections. J Struct Eng ASCE 2005;131:1738–45.
[112] Woo Y, Hwang T, Oh I, Seo D, Moon Y. Analysis on selective laser melting of WC-reinforced H13 steel composite powder by finite element method. Adv Mech Eng 2018;11:1–11.
[113] Bartsch K, Herzog D, Bossen B, Emmelmann C. Material modeling of Ti6Al4V alloy processed by laser powder bed fusion for application in macro-scale process simulation. Mater Sci Eng 2021;814:141237.